Materials Today Communications 58 (2027) 116713

Contents lists available at ScienceDirect

Materials Today Communications

journal homepage: www.elsevier.com/locate/mtcomm

# Band-alignment engineering of cadmsium-free $Sb_2Se_3$ thin-film solar cells using composition-tuned $In_2(O_{1-x},S_x)_3$ buffer layers

Danial Keighobadi [a], Mehdi Mousavi-Kamazani [b], Mohammad Danaie [a,*]

[a] Faculty of Electrical and Computer Engineering, Semnan University, Semnan, Iran
[b] Department of Nanotechnology, Faculty of New Sciences and Technologies, Semnan University, Semnan, Iran

ARTICLE INFO

*Keywords:*
Sb2Se3 thin-film solar cells
Cd-free buffer layer
In2(O1 −x,Sx)3
Band-alignment engineering
Conduction-band offset
SCAPS-1D simulation
Interface recombination
Photovoltaic performance

ABSTRACT

Cadmium-free buffer-layer engineering is a critical route toward improving both the environmental compatibility and photovoltaic performance of $Sb_2Se_3$ thin-film solar cells. In this work, a calibrated SCAPS-1D numerical framework was employed to investigate composition-dependent band-alignment engineering in Mo/$MoSe_2$/$Sb_2Se_3$/$In_2(O_{1-x},S_x)_3$/ZnO/Al:ZnO solar cells, using the conventional Mo/$MoSe_2$/$Sb_2Se_3$/CdS/ZnO/Al:ZnO architecture as the reference device. The simulation model was first validated against reported experimental external quantum efficiency, integrated short-circuit current density, light-intensity-dependent short-circuit current density, and current-voltage characteristics, confirming the reliability of the adopted optical and electrical framework. Subsequently, the composition of the $In_2(O_{1-x},S_x)_3$ buffer layer was systematically varied, where x = S/(O+S) and 1-x = O/(O+S) represents the corresponding oxygen fraction. A physically constrained composition-guided parameterization was employed to investigate how oxygen incorporation modifies the buffer-layer bandgap, effective electron affinity, and conduction-band offset with $Sb_2Se_3$. Within the investigated parameter range, increasing the oxygen fraction widened the modeled buffer-layer bandgap from 1.92 to 3.05 eV and reduced its effective electron affinity from 4.30 to 3.90 eV, thereby shifting the $Sb_2Se_3$/buffer conduction-band offset from a pronounced cliff-like alignment of −0.26 eV toward a nearly flat configuration and subsequently to a spike-like alignment of + 0.14 eV. The optimum modeled condition corresponds to $In_2S_{2.685}O_{0.315}$, for which x = 0.895 and the oxygen fraction is 1-x = 0.105. This composition yields an almost flat conduction-band offset of approximately −0.01 eV, providing a favorable balance between suppression of interfacial recombination and efficient electron extraction. The optimized Cd-free device exhibited $V_{oc}$= 0.771 V, $J_{sc}$= 34.25 mA $cm^{-2}$, FF= 72.43%, and a power conversion efficiency of 19.12%, compared with 0.480 V, 30.87 mA $cm^{-2}$, 67.18%, and 10.12%, respectively, for the CdS-based reference cell. The enhanced device performance was further supported by improved spectral response, reduced capacitive charge accumulation, increased built-in potential, and enhanced recombination resistance. These findings demonstrate the potential of composition-engineered $In_2(O_{1-x},S_x)_3$ as a Cd-free buffer layer for $Sb_2Se_3$ thin-film solar cells and highlight the importance of controlled band-edge modulation for simultaneously reducing optical losses and suppressing interface recombination. The identified composition should be regarded as a modeling-based design target whose precise composition-property relationship requires subsequent experimental verification.

## 1. Introduction

The transition toward low-carbon energy systems has intensified the demand for photovoltaic technologies that combine high efficiency, low manufacturing cost, material abundance, and environmental compatibility [1–4]. Although established thin-film technologies such as CdTe and Cu(In,Ga)$Se_2$ have reached advanced levels of device performance, their large-scale deployment is still accompanied by concerns related to elemental scarcity, toxicity, process complexity, and long-term sustainability [5–9]. These limitations have stimulated extensive research into emerging absorber materials capable of delivering strong light harvesting and favorable electronic transport while relying on simpler, more abundant, and less hazardous chemical compositions [10–13].

Environmental compatibility has also become an increasingly important consideration in emerging photovoltaic technologies, particularly in perovskite solar cells, where the replacement of toxic Pb-

* Corresponding author.
*E-mail address:* danaie@semnan.ac.ir (M. Danaie).

https://doi.org/10.1016/j.mtcomm.2026.116713
Received 14 July 2026; Received in revised form 8 November 2026; Accepted 19 November 2026
Available online 22 November 2026
2352-4928/© 2026 The Author(s). Published by Elsevier Ltd. This is an open access article under the CC BY-NC license (http://creativecommons.org/licenses/by-nc/4.0/).

containing absorbers has stimulated extensive research into lead-free alternatives. Recent numerical studies have demonstrated the potential of non-toxic perovskite compositions and simplified device architectures for simultaneously improving sustainability and photovoltaic performance. For example, Yaqub et al. investigated an economic HTL-free solar-cell architecture based on the lead-free double perovskite $Cs_2AgBiBr_6$ and demonstrated that appropriate optimization of the transport layers, absorber properties, defect density, and contact configuration can substantially improve device performance [14]. Similarly, Khatoon et al. investigated an all-inorganic lead-free $CsSnBr_3$ perovskite solar cell using SCAPS-1D, employing $SnO_2$ and CuI as the electron- and hole-transport layers, respectively, and demonstrated the importance of layer-thickness, defect-density, and interface optimization for achieving enhanced photovoltaic characteristics [15]. These developments illustrate a broader trend in photovoltaic materials research in which high conversion efficiency must be pursued together with reduced toxicity, improved stability, and environmentally responsible material selection. The same sustainability-driven design principle motivates the development of Cd-free buffer layers for $Sb_2Se_3$ thin-film solar cells, where the replacement of conventional CdS should ideally eliminate hazardous Cd without compromising, and preferably while improving, heterojunction performance.

Antimony selenide ($Sb_2Se_3$) has emerged as one of the most promising absorber candidates for next-generation thin-film solar cells [16–20]. Its simple binary composition, earth-abundant constituents, high optical absorption coefficient, excellent chemical stability, and suitable bandgap for single-junction photovoltaics make it highly attractive for scalable device development [21–23]. In addition, the quasi-one-dimensional crystal structure of $Sb_2Se_3$ can provide preferential carrier-transport pathways when the absorber orientation is properly controlled. However, this structural anisotropy also makes the photovoltaic response highly sensitive to interface quality, defect-assisted recombination, and junction energetics [24,25]. Consequently, the performance of $Sb_2Se_3$ solar cells are often limited not by optical absorption alone, but by non-ideal charge separation and recombination losses at the absorber/buffer interface [22,26–28].

In conventional $Sb_2Se_3$ thin-film solar cells, CdS is commonly used as the n-type buffer layer because of its mature processing, chemical compatibility, and electron-selective behavior [29–32]. Nevertheless, CdS imposes two major constraints on sustainable and high-performance device design. First, the use of cadmium is environmentally undesirable and raises toxicity-related concerns. Second, the moderate bandgap of CdS results in parasitic absorption in the short-wavelength region, reducing the photon flux reaching the $Sb_2Se_3$ absorber. The transmitted photon flux through the buffer layer can be described as:

$$\Phi_{tr}(\lambda) = \Phi_0(\lambda) \quad \exp[-\alpha b(\lambda) d_b] \tag{1}$$

where $\Phi_{tr}(\lambda)$ is the transmitted photon flux, $\Phi_0(\lambda)$ is the incident photon flux, $\alpha_b(\lambda)$ is the wavelength-dependent optical absorption coefficient of the buffer layer, and $d_b$ is the buffer-layer thickness.

This relation indicates that a buffer layer with a lower absorption coefficient and wider optical bandgap can reduce front-side optical losses and improve the short-wavelength contribution to the external quantum efficiency and short-circuit current density.

Beyond optical transparency, the electronic alignment between $Sb_2Se_3$ and the buffer layer is equally decisive. The conduction-band offset at the absorber/buffer interface can be estimated from the electron affinities of the two semiconductors [33–35]:

$$\Delta E_c = \chi_{Sb_2Se_3} - \chi_{buffer} \tag{2}$$

where $\Delta E_c$ is the conduction-band offset, $\chi Sb_2Se_3$ is the electron affinity of $Sb_2Se_3$, and $\chi_{buffer}$ is the electron affinity of the buffer layer. A negative $\Delta E_c$ produces a cliff-like alignment, which enhances interfacial recombination by lowering the energetic barrier against electron-hole recombination near the junction. In contrast, an excessively positive $\Delta E_c$ forms a spike-like barrier that can impede electron extraction and deteriorate the fill factor. Therefore, the optimum buffer layer should provide a nearly flat or slightly positive conduction-band offset, where interfacial recombination is suppressed without introducing a severe transport barrier [36–41].

The influence of interface recombination on the open-circuit voltage can be understood through the diode relation:

$$V_{oc} = \left(n\frac{k_B T}{q}\right)\ln\left[\left(\frac{J_{sc}}{J_0}\right)+1\right] \tag{3}$$

where n is the diode ideality factor, $k_B$ is the Boltzmann constant, T is the absolute temperature, q is the elementary charge, $J_{sc}$ is the short-circuit current density, and $J_0$ is the reverse saturation current density.

Since $J_0$ is strongly governed by bulk and interfacial recombination pathways, reducing recombination at the $Sb_2Se_3$/buffer interface is essential for increasing the quasi-Fermi-level splitting and improving $V_{oc}$. Accordingly, an effective Cd-free buffer layer must simultaneously minimize optical absorption losses, optimize band alignment, and suppress defect-assisted interfacial recombination.

$In_2S_3$ has been widely considered as a promising Cd-free buffer material for chalcogenide thin-film solar cells because of its n-type conductivity, relatively wide bandgap, and chemical compatibility with absorber layers. However, pristine $In_2S_3$ does not necessarily provide the optimum conduction-band alignment with $Sb_2Se_3$. A particularly effective route to overcome this limitation is oxygen alloying, in which sulfur is partially substituted by oxygen to form $In_2(O,S)_3$. By controlling the oxygen-to-anion ratio,

$$x \quad = \frac{S}{O+S} \tag{4}$$

the bandgap and electron affinity of the buffer layer can be systematically modulated. Increasing the oxygen content widens the buffer-layer bandgap and decreases its electron affinity, enabling a controlled transition of the $Sb_2Se_3/In_2(O,S)_3$ interface from cliff-like alignment to nearly flat alignment and eventually to spike-like alignment. This compositional tunability provides a direct link between material chemistry and device-level performance, because the oxygen fraction simultaneously influences optical transmission, conduction-band offset, interfacial recombination, carrier extraction, built-in potential, and spectral response.

Numerical device simulation provides an efficient route to identify such coupled optical and electronic effects before experimental fabrication. In this work, SCAPS-1D is used as a physically based simulation platform to evaluate conventional and Cd-free $Sb_2Se_3$ solar cells. To ensure predictive reliability, the model is first calibrated against reported experimental data for the conventional Mo/$MoSe_2$/$Sb_2Se_3$/CdS/ZnO/Al:ZnO architecture, including external quantum efficiency, integrated $J_{sc}$, light-intensity-dependent $J_{sc}$ , and current-voltage characteristics. This validation step ensures that the selected optical and electrical parameters realistically describe the reference device before being extended to the proposed Cd-free configuration.

Herein, a composition-tuned $In_2(O_{1-x},S_x)_3$ buffer layer is introduced as a Cd-free replacement for CdS in $Sb_2Se_3$ thin-film solar cells. The oxygen content is systematically varied to regulate the buffer-layer bandgap, electron affinity, and conduction-band offset with $Sb_2Se_3$. The optimized $In_2S_{2.685}O_{0.315}$ composition, corresponding to (x = 0.895, corresponding to an oxygen fraction of 1-x = 0.105), produces an almost flat conduction-band offset, thereby suppressing cliff-induced interface recombination while preserving efficient electron extraction. Compared with the calibrated CdS-based reference device, the optimized Cd-free architecture exhibits substantially enhanced $V_{oc}$, $J_{sc}$, fill factor, and power conversion efficiency. This study therefore establishes a composition-resolved design strategy in which oxygen-alloyed $In_2(O,S)_3$ simultaneously reduces optical losses, improves interfacial band alignment, strengthens carrier selectivity, and advances

the development of environmentally sustainable high-performance $Sb_2Se_3$ thin-film solar cells.

## 2. Device configuration and simulation methodology

The photovoltaic characteristics of the conventional and Cd-free $Sb_2Se_3$ thin-film solar cells were numerically investigated using SCAPS-1D. The simulated device architectures are schematically illustrated in Fig. 1. The reference cell, shown in Fig. 1(a), consists of the Mo/$MoSe_2$/$Sb_2Se_3$/CdS/ZnO/Al:ZnO stack, whereas the proposed Cd-free architecture, shown in Fig. 1(b), replaces the conventional CdS buffer with a composition-engineered $In_2(O_{1-x},S_x)_3$ layer, giving the structure Mo/$MoSe_2$/$Sb_2Se_3$/$In_2(O_{1-x},S_x)_3$/ZnO/Al:ZnO. In both configurations, $Sb_2Se_3$ serves as the p-type absorber, ZnO and Al:ZnO act as the electron-transport/window layers, Mo is used as the rear metallic contact, and the ultrathin $MoSe_2$ interfacial layer is incorporated at the back side to improve rear-contact selectivity and mitigate recombination losses at the Mo/$Sb_2Se_3$ interface.

The ultrathin $MoSe_2$ interlayer plays an important role in controlling the electronic properties of the rear contact. For the p-type $Sb_2Se_3$ absorber, an effective rear contact should facilitate majority-carrier (hole) extraction while limiting minority-electron recombination at the metal/semiconductor interface. The insertion of $MoSe_2$ between $Sb_2Se_3$ and Mo reduces the direct electronic interaction of the absorber with the metallic contact and promotes a more favorable, quasi-ohmic contact configuration, thereby lowering the effective rear-contact barrier and facilitating hole transport toward the Mo electrode [42,43]. At the same time, the interfacial layer improves carrier selectivity by reducing the probability of minority electrons reaching recombination-active states at the rear electrode. The very small $MoSe_2$ thickness used in the present model (0.002 $\mu$m) is intended to provide this interfacial modification without introducing a significant additional transport resistance. It should be emphasized that the $MoSe_2$ layer and its parameters were kept identical in both the CdS-based reference and Cd-free devices; therefore, the comparative performance enhancement discussed in this work originates from the composition-dependent modification of the front $Sb_2Se_3$/buffer heterointerface rather than from changes in the rear-contact configuration.

The material parameters employed for the baseline $Sb_2Se_3$/CdS device are summarized in Table 1. The $Sb_2Se_3$ absorber thickness was fixed at 2.6 $\mu$m [1–3,44], while the thicknesses of CdS, ZnO, Al:ZnO, and $MoSe_2$ were set to 0.06, 0.1, 0.3, and 0.002 $\mu$m, respectively. The $Sb_2Se_3$ absorber was modeled as a p-type semiconductor with a bandgap of 1.20 eV, electron affinity of 4.04 eV, relative dielectric permittivity of 19, electron mobility of 15 $cm^2\ V^{-1}\ s^{-1}$, hole mobility of 5.1 $cm^2\ V^{-1}\ s^{-1}$, and acceptor concentration of $7\times\ 10^{15} cm^{-3}$. The CdS buffer was defined as an n-type layer with a bandgap of 2.42 eV and electron affinity of 4.45 eV. ZnO and Al:ZnO were introduced as wide-band-gap n-type front layers with bandgaps of 3.30 and 3.60 eV, respectively. These parameters were adopted from experimentally supported values and used as the reference input set for model calibration.

For the Cd-free architecture, the CdS buffer was replaced by $In_2(O_{1-x},S_x)_3$, and the oxygen content was varied according to the composition-dependent parameters listed in Table 2. Increasing the

**Table 1**
Material parameters used in the SCAPS-1D simulation for the proposed and conventional $Sb_2Se_3$-based solar cells [45,46].

| Parameters | $Sb_2Se_3$ | CdS | ZnO | ZnO: Al | $MoSe_2$ |
|---|---|---|---|---|---|
| Thickness ($\mu$m) | 2.6 | 0.06 | 0.1 | 0.3 | 0.002 |
| $E_g$ (eV) | 1.2 | 2.42 | 3.3 | 3.6 | 1.4 |
| $\chi_e$ (eV) | 4.04 | 4.45 | 4.5 | 4.5 | 4.32 |
| $\varepsilon_r$ | 19 | 10 | 9 | 9 | 7.29 |
| $N_c$ ($cm^{-3}$) | $1\times10^{19}$ | $2.2\times10^{18}$ | $2.2\times10^{18}$ | $2.2\times10^{18}$ | $9\times10^{18}$ |
| $N_v$ ($cm^{-3}$) | $1\times10^{19}$ | $1.8\times10^{19}$ | $1.8\times10^{19}$ | $1.8\times10^{19}$ | $9\times10^{18}$ |
| $v_{th,e}$ ($cm/s$) | $10^7$ | $10^7$ | $10^7$ | $10^7$ | $10^7$ |
| $v_{th,h}$ ($cm/s$) | $10^7$ | $10^7$ | $10^7$ | $10^7$ | $10^7$ |
| $\mu_e$ ($cm^2/Vs$) | 15 | 100 | 100 | 100 | 25 |
| $\mu_h$ ($cm^2/Vs$) | 5.1 | 25 | 25 | 25 | 100 |
| Doping ($cm^{-3}$) | $7\times10^{15}$ (A) | $7.12\times10^{17}$ (D) | $6.77\times10^{18}$ (D) | $10^{20}$ (D) | $5\times10^{19}$ (A) |

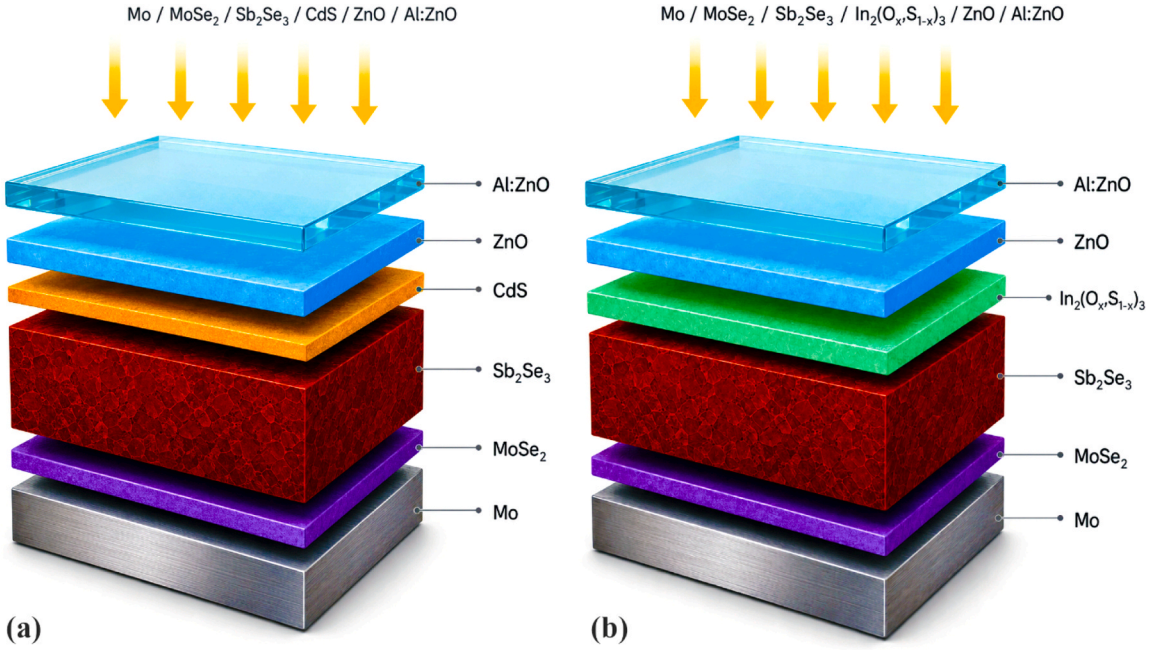


**Fig. 1.** Schematic configuration of the investigated $Sb_2Se_3$ thin-film solar cells. (a) Conventional reference device with the Mo/$MoSe_2$/$Sb_2Se_3$/CdS/ZnO/Al:ZnO architecture. (b) Proposed Cd-free device in which the CdS buffer layer is replaced by a composition-tuned $In_2(O_{1-x},S_x)_3$ buffer layer. The modified buffer layer is introduced to improve optical transparency, tune the absorber/buffer band alignment, and suppress interfacial recombination losses.

**Table 2**
Composition-dependent physical parameters of $In_2(O,S)_3$ buffer layer used in SCAPS simulation [47–52].

| Approximate composition | O/(O+S) ratio, 1-x | S:O ratio | $E_g$ (eV) | $\chi$ of $In_2(O,S)_3$ (eV) | $\Delta E_c$ with $Sb_2Se_3$ (eV) | Band alignment |
|---|---|---|---|---|---|---|
| $In_2S_3$ | 0.000 | 100:0 | 1.92 | 4.3 | −0.26 | Pronounced Cliff |
| $In_2S_{2.91}O_{0.09}$ | 0.030 | 97:3 | 2.10 | 4.22 | −0.18 | Cliff |
| $In_2S_{2.85}O_{0.15}$ | 0.050 | 95:5 | 2.25 | 4.16 | −0.12 | Cliff |
| $In_2S_{2.79}O_{0.21}$ | 0.070 | 93:7 | 2.4 | 4.11 | −0.07 | Slight Cliff |
| $In_2S_{2.73}O_{0.27}$ | 0.090 | 91:9 | 2.55 | 4.07 | −0.03 | Nearly Flat |
| **$In_2S_{2.685}O_{0.315}$** | **0.105** | **89.5:10.5** | **2.7** | **4.05** | **−0.01** | **Nearly Flat/Optimum** |
| $In_2S_{2.64}O_{0.36}$ | 0.120 | 88:12 | 2.85 | 3.98 | + 0.06 | Small Spike |
| $In_2S_{2.58}O_{0.42}$ | 0.140 | 86:14 | 3.05 | 3.90 | + 0.14 | Spike |

oxygen fraction modifies the buffer-layer bandgap and electron affinity, thereby allowing the $Sb_2Se_3/In_2(O,S)_3$ interfacial energetics to be tuned from cliff-like to nearly flat and then spike-like alignment. This compositional strategy was used to isolate the role of buffer-layer chemistry in controlling interfacial recombination, carrier extraction, and photovoltaic performance while keeping the remaining device structure unchanged.

SCAPS-1D evaluates the solar-cell response by solving the coupled electrostatic and carrier-transport equations under the specified material, defect, interface, and contact parameters. The electrostatic potential distribution across the multilayer device is governed by the one-dimensional Poisson equation:

$$\frac{d}{dx}\left[\frac{\varepsilon(x)d\psi(x)}{dx}\right] = -q\left[p(x) - n(x) + N_D^+(x) - N_A^-(x) + N_t(x)\right] \quad (5)$$

where $\varepsilon(x)$ is the dielectric permittivity, $\psi(x)$ is the electrostatic potential, q is the elementary charge, p(x) and n(x) are the hole and electron concentrations, $N_D^+(x)$ and $N_A^-(x)$ are the ionized donor and acceptor densities, and $N_t(x)$ denotes the defect-related charge density. This equation determines the built-in potential and electric-field distribution responsible for photocarrier separation across the heterojunction.

Carrier transport was described using the drift-diffusion current equations:

$$J_n = q\,\mu_n\,n\,E + q\,D_n\frac{dn}{dx} \quad (6)$$

$$J_p = q\,\mu_p\,p\,E - q\,D_p\frac{dp}{dx} \quad (7)$$

where $J_n$ and $J_p$ are the electron and hole current densities, $\mu_n$ and $\mu_p$ are the electron and hole mobilities, $D_n$ and $D_p$ are the corresponding diffusion coefficients, and E is the internal electric field. These equations account for both field-driven drift and concentration-gradient-driven diffusion transport.

The carrier-conservation conditions were expressed through the electron and hole continuity equations:

$$\frac{dJ_n}{dx} = q[R(x) - G(x)] \quad (8)$$

$$\frac{dJ_p}{dx} = q[G(x) - R(x)] \quad (9)$$

where G(x) is the optical generation rate and R(x) is the total recombination rate. Among the recombination pathways, defect-assisted Shockley-Read-Hall recombination is particularly important for $Sb_2Se_3$ heterojunctions because deep states and interfacial traps can strongly reduce the quasi-Fermi-level splitting. The SRH recombination rate is given by:

$$R_{SRH} = \frac{\left[n_p - n_i^2\right]}{\left[\tau_p(n + n_1) + \tau_n(p + p_1)\right]} \quad (10)$$

where (n) and (p) are the electron and hole concentrations, $n_i$ is the intrinsic carrier concentration, $\tau_n$ and $\tau_p$ are the electron and hole lifetimes, and $n_1$ and $p_1$ are trap-dependent carrier concentrations. Inclusion of this recombination formalism enables the simulation to capture the effect of defect-mediated losses at the absorber bulk and absorber/buffer interface.

To provide a complete description of the recombination model and improve the reproducibility of the numerical analysis, bulk and interfacial defect states were explicitly considered within the Shockley-Read-Hall (SRH) formalism. A neutral single-level defect distribution was adopted for the semiconductor layers. The bulk defect density of the $Sb_2Se_3$ absorber was taken as ($10^{14}$ $cm^{-3}$), with the defect level located at ($E_V$ +0.60) eV. For CdS and composition-engineered $In_2(O_{1-x},S_x)_3$, a bulk defect density of ($10^{15}$ $cm^{-3}$) was considered. The CdS trap level was positioned near the middle of its bandgap at ($E_V$ +1.21) eV, whereas the defect level in $In_2(O_{1-x},S_x)_3$ was defined at approximately mid-gap and therefore followed the composition-dependent band-gap variation. Bulk defect densities of ($10^{15}$ $cm^{-3}$) were also considered for ZnO and Al:ZnO, with representative trap positions of ($E_V$ +1.65) and ($E_V$ +1.80) eV, respectively. For the ultrathin $MoSe_2$ rear interlayer, a defect density of ($10^{14}$ $cm^{-3}$) with a defect level at ($E_V$ +0.70) eV was assumed. For all bulk defect states, electron and hole capture cross-sections of ($10^{-15}$ $cm^2$) were employed.

Interface recombination was independently described using two-dimensional SRH interface states. To permit a physically consistent comparison between the conventional and Cd-free architectures, an interface defect density of ($10^{11}$ $cm^{-2}$) was considered at both the $Sb_2Se_3$/CdS and $Sb_2Se_3/In_2(O_{1-x},S_x)_3$ heterointerfaces, with neutral single-level states located approximately near the mid-gap of $Sb_2Se_3$ and electron and hole capture cross-sections of ($10^{-15}$ $cm^2$). Lower interface-state densities of ($10^{10}$ $cm^2$) were considered at the $Sb_2Se_3/MoSe_2$ rear interface and the buffer/ZnO interface. Importantly, the absorber/buffer interface defect density and carrier-capture cross-sections were kept identical when comparing the CdS reference cell with the composition-engineered $In_2(O,S)_3$ devices. Therefore, the predicted reduction in heterointerface recombination was not generated by imposing an artificially lower trap density for the optimized device. Instead, it originates from the composition-dependent modification of the buffer electron affinity and conduction-band offset, which changes the local carrier population and consequently the SRH recombination probability at the heterojunction.

The numerical calculations were performed at 300 K under standard AM1.5 G illumination with an incident optical power density of 100 mW $cm^{-2}$ (1 sun), incident from the Al:ZnO front-contact side. Electron and hole thermal velocities of ($10^7$ $cm.s^{-1}$) were considered in the defect-assisted recombination calculations. The rear Mo contact was represented using a work function of approximately 5.30 eV, while the front contact was treated as an electron-selective quasi-ohmic contact with a representative work function of approximately 4.40 eV. Electron and hole surface recombination velocities of ($10^7$ $cm.s^{-1}$) were used as the contact-boundary values. The simulations were performed using SCAPS-1D 3.3.11. All optical, electrical, defect, interface, and contact parameters other than the explicitly composition-dependent properties of the $In_2(O_{1-x},S_x)_3$ buffer were maintained consistently during the oxygen-composition sweep so that the influence of band-alignment

engineering could be evaluated independently.

The optical response of the composition-engineered $In_2(O_{1-x},S_x)_3$ buffer was described using wavelength-dependent absorption coefficients rather than by treating the bandgap as the sole optical parameter. The adopted optical behavior was anchored to experimentally reported transmission/reflection measurements of $\beta$-$In_2S_{3-3x}O_{3x}$ thin films, from which the absorption coefficient $\alpha(\lambda)$ was determined as a function of wavelength. These experimental studies demonstrate that oxygen incorporation modifies not only the optical bandgap but also the complete absorption edge, producing a progressive displacement of the strong-absorption region toward higher photon energies. For simulated oxygen ratios located between experimentally characterized compositions, $\alpha(\lambda)$ was estimated by composition interpolation using:

$$\alpha(\lambda,x) = \alpha(\lambda,x_1) + [(x-x_1)/(x_2-x_1)] \times [\alpha(\lambda,x_2) - \alpha(\lambda,x_1)] \quad (11)$$

where $x_1$ and $x_2$ denote the nearest experimentally characterized oxygen compositions. This approach preserves the wavelength dependence of the experimentally observed absorption response while providing optical profiles for the intermediate compositions investigated numerically. The band-gap values listed for the different $In_2(O,S)_3$ compositions therefore describe the evolution of the absorption threshold, whereas the wavelength-dependent $\alpha(\lambda)$ profiles determine the actual optical attenuation used in the device analysis. Because experimentally measured optical constants can vary with deposition method, crystallinity, phase distribution, and oxygen incorporation, the adopted spectra are considered experimentally anchored representative optical inputs rather than universal optical constants of $In_2(O,S)_3$.

The optical generation profile was calculated from the wavelength-dependent absorption in the multilayer stack and then coupled to the electrical transport solution. After self-consistent convergence of the electrostatic potential, carrier densities, current densities, and recombination rates, the J-V characteristics and photovoltaic output parameters were extracted under standard illumination. This framework allows changes in buffer-layer composition to be connected directly with variations in built-in field, recombination current, carrier-collection efficiency, $V_{oc}$, $J_{sc}$, FF, and PCE.

In general, the simulation strategy was designed to isolate the role of oxygen-alloyed $In_2(O,S)_3$ buffer layers in Cd-free $Sb_2Se_3$ solar cells. The parameters in Table 1 define the calibrated $Sb_2Se_3$/CdS reference architecture, whereas Table 2 provides the composition-dependent optical and electronic parameters of the $In_2(O,S)_3$ buffer. By varying only the oxygen content after model calibration, the effects of band-gap widening, electron-affinity reduction, interfacial energetics, charge-selective transport, and recombination suppression can be directly correlated with the resulting photovoltaic response [47–49,53,54].

## 3. Results and discussion

### 3.1. Calibration and validation of the SCAPS-1D model

Prior to assessing the proposed Cd-free architecture, the SCAPS-1D model was calibrated against the reported experimental response of the conventional Mo/$MoSe_2$/$Sb_2Se_3$/CdS/ZnO/Al:ZnO reference device. This step is critical because the reliability of any simulation-based optimization depends on whether the selected optical, electrical, defect, and interface parameters can reproduce the experimentally observed behavior of the baseline cell. The calibration was therefore evaluated using three complementary criteria: spectral response, illumination-dependent photocurrent, and illuminated current-voltage characteristics, as shown in Fig. 2.

Fig. 2(a) compares the experimental and simulated external quantum efficiency spectra together with the corresponding integrated short-circuit current density. The close overlap between the measured and calculated EQE curves confirms that the calibrated model accurately captures wavelength-dependent absorption, carrier generation, and

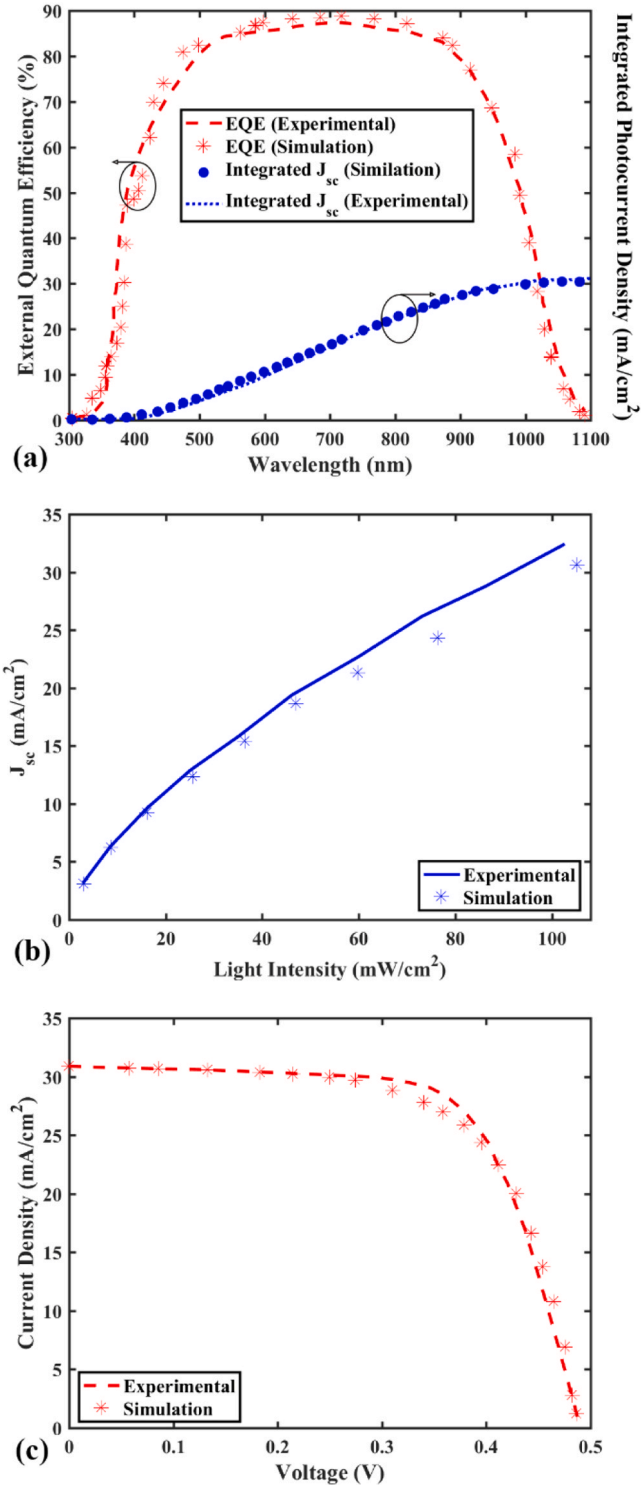


**Fig. 2.** Calibration and validation of the SCAPS-1D model against reported experimental data for the conventional $Sb_2Se_3$/CdS reference solar cell [55]. (a) Experimental and simulated external quantum efficiency spectra together with the corresponding integrated short-circuit current density. (b) Experimental and simulated variation of $J_{sc}$ as a function of illumination intensity. (c) Comparison between experimental and simulated current-voltage characteristics under standard illumination. The close agreement confirms the reliability of the calibrated model for further buffer-layer optimization.

collection probability in the reference $Sb_2Se_3$/CdS device. In the short-wavelength region, the EQE is mainly controlled by optical attenuation in the front window/buffer stack and by carrier collection near the CdS/$Sb_2Se_3$ heterojunction. By contrast, the long-wavelength response is governed by absorption deeper inside the $Sb_2Se_3$ absorber, where carrier diffusion length and bulk recombination become more influential. Therefore, the agreement over the full spectral range indicates that the optical constants, layer thicknesses, and transport parameters used in the model are physically consistent with the experimental device.

The integrated photocurrent was evaluated from the simulated EQE according to:

$$J_{sc,EQE} = q \int \Phi AM1.5G(\lambda) \times EQE(\lambda) d\lambda \tag{12}$$

where $J_{sc}$ ,EQE is the EQE-derived short-circuit current density, q is the elementary charge, $\Phi_{AM1.5}G(\lambda)$ is the incident photon flux under AM1.5 G illumination, and $EQE(\lambda)$ is the external quantum efficiency at wavelength $\lambda$. The agreement between the integrated simulated current and the experimental trend confirms that the model does not merely reproduce the spectral shape, but also provides a reliable estimate of the total collectable photocurrent.

Fig. 2(b) shows the variation of $J_{sc}$ with incident light intensity. The simulated data closely reproduce the experimental trend over the investigated illumination range, indicating that the calibrated model captures the light-dependent balance between photogeneration, carrier transport, and collection. The dependence of $J_{sc}$ on illumination intensity can be described by the power-law relation:

$$\boldsymbol{J_{sc} \propto I^{\gamma}} \tag{13}$$

where I is the incident light intensity and γ is the photocurrent-light-intensity exponent. The exponent was determined from the slope of the log ($J_{sc}$) versus log(I) relationship. The extracted values are $\gamma_{exp} \approx 0.664$ for the experimental data and $\gamma_{sim} \approx 0.657$ for the simulated data, demonstrating excellent agreement between experiment and simulation. Both values are approximately 0.66 and therefore indicate a sublinear photocurrent response rather than an ideal linear dependence. A value of $\gamma = 1$ would correspond to $J_{sc}$ increasing directly in proportion to photon flux under essentially loss-free collection conditions, whereas $\gamma < 1$ indicates that the increase in collected photocurrent becomes progressively weaker at higher illumination intensities because of recombination and/or transport-related limitations. The close correspondence between the experimental and simulated $\gamma$ values therefore provide an additional quantitative validation of the recombination and carrier-transport treatment employed in the calibrated SCAPS-1D model.

Fig. 2(c) compares the experimental and simulated J-V characteristics under standard illumination. The strong agreement between the two curves demonstrates that the calibrated model reproduces the main photovoltaic parameters of the reference device, including $V_{oc}$, $J_{sc}$, FF, and PCE. Unlike the EQE spectrum, which mainly probes wavelength-dependent generation and collection, the J-V response reflects the combined influence of junction electrostatics, recombination current, carrier-selective transport, series resistance, and shunt leakage. The illuminated diode behavior may be represented as [56]:

$$J(V) = J_0 \left[ \exp\left( \frac{qV}{nk_BT} \right) - 1 \right] - J_{ph} \tag{14}$$

where $J_0$ is the reverse saturation current density, n is the ideality factor, $k_B$ is the Boltzmann constant, T is the absolute temperature, and $J_{ph}$ is the photogenerated current density. The ability of the simulation to reproduce the experimental J-V curve therefore confirms that the recombination and transport parameters are sufficiently realistic for subsequent device optimization.

As a whole, the simultaneous agreement in Fig. 2(a)-(c) verifies that the calibrated SCAPS-1D model provides a credible baseline for evaluating Cd-free buffer-layer engineering. After this validation, CdS was replaced by composition-tuned $In_2(O,S)_3$ while keeping the remaining device architecture unchanged. This strategy enables the isolated analysis of how oxygen alloying modifies absorber/buffer band alignment, optical response, interfacial recombination, and photovoltaic output.

### 3.2. Composition-dependent band alignment and optical response of $In_2(O,S)_3$ buffer layers

After model validation, the CdS buffer was replaced with $In_2(O,S)_3$ to examine how oxygen alloying modifies the $Sb_2Se_3$/buffer heterointerface. The composition-dependent parameters listed in Table 2 show that increasing the oxygen content from 1-x = 0–1-x = 0.14 changes the buffer from $In_2S_3$ to $In_2S_{2.58}O_{0.42}$. This compositional evolution simultaneously increases the optical bandgap from 1.92 to 3.05 eV and decreases the electron affinity from 4.30 to 3.90 eV. Therefore, oxygen incorporation provides a direct route to tune both the optical transparency and the electronic band discontinuity of the buffer layer.

The conduction-band offset values in Table 2 reveal a systematic transition in the $Sb_2Se_3$/$In_2(O,S)_3$ interface. For pure $In_2S_3$, the offset is −0.26 eV, corresponding to a severe cliff-like alignment. Such a pronounced negative CBO is unfavorable because it reduces the energetic barrier against interfacial electron-hole recombination and increases the recombination current at the heterojunction. The associated voltage loss can be qualitatively related to the recombination current through:

$$\Delta V_{oc} \approx \left( \frac{k_BT}{q} \right) \ln \left( \frac{J_{0,high}}{J_{0,low}} \right) \tag{15}$$

where $\Delta V_{oc}$ is the open-circuit-voltage gain achieved by reducing recombination, $J_{0,high}$ is the larger saturation current associated with stronger recombination, and $J_{0,low}$ is the reduced saturation current after interface optimization. This relation highlights why suppressing the cliff-induced recombination current is essential for improving $V_{oc}$.

As the oxygen content increases, the negative offset becomes progressively smaller. The conduction-band offset changes from −0.18 eV at 1-x = 0.03 to −0.12 eV at 1-x = 0.05 and −0.07 eV at 1-x = 0.07. Although these compositions still produce cliff-like alignment, the reduced cliff depth indicates a gradual improvement in interfacial energetics. At 1-x = 0.09, the offset reaches −0.03 eV, representing only a slight cliff. The optimum condition is obtained for $In_2S_{2.685}O_{0.315}$, corresponding to 1-x = 0.105, where the conduction-band offset becomes −0.01 eV. This nearly flat alignment is electronically favorable because it suppresses cliff-assisted interface recombination while preserving barrier-free electron extraction from $Sb_2Se_3$ to the front transport layers.

It is important to emphasize that maintaining the same interface-defect density does not imply an identical interface-recombination rate. Within the SRH formalism, recombination is determined not only by the density and capture cross-sections of the defect states but also by the local electron and hole concentrations at the heterointerface. Consequently, modification of the conduction-band offset can substantially change the recombination rate even when the microscopic trap population is kept unchanged. In the CdS-based reference device, the less favorable absorber/buffer energetics promote a larger simultaneous population of electrons and holes in the junction region, increasing the probability of trap-assisted recombination. Oxygen incorporation into $In_2(O_{1-x},S_x)_3$ progressively decreases the buffer electron affinity and modifies the conduction-band alignment. At the optimized composition (1-x = 0.105), corresponding to $In_2S_{2.685}O_{0.315}$, the conduction-band offset approaches −0.01 eV. This nearly flat configuration reduces minority-carrier accumulation at the interface and hence decreases the SRH recombination probability without requiring an assumed reduction in interface trap density. The resulting decrease in recombination current increases the quasi-Fermi-level splitting and accounts primarily for the pronounced increase in ($V_{oc}$) from 0.480 to 0.771 V. Simultaneously,

improved carrier selectivity and electron extraction increase the FF from 67.18% to 72.43%, while the wider buffer bandgap and reduced parasitic absorption contribute to the increase in ($J_{sc}$) from 30.87 to 34.25 mA $cm^{-2}$. Thus, the predicted increase in PCE from 10.12% to 19.12% results from the coupled improvement of heterojunction energetics, recombination suppression, carrier transport, and optical transmission rather than from an artificially improved defect quality assigned to the optimized device [30].

Further oxygen incorporation shifts the $Sb_2Se_3/In_2(O,S)_3$ heterointerface from a nearly flat conduction-band alignment toward an increasingly positive spike-like configuration.

Further oxygen incorporation shifts the heterointerface toward a positive spike-like conduction-band alignment. At 1-x = 0.12, the offset becomes + 0.06 eV, which may still be acceptable because a small spike can suppress recombination without significantly blocking electron transport. However, at 1-x = 0.14, the offset increases to + 0.14 eV. Such a larger spike can act as an electron-extraction barrier. The probability of thermally assisted electron transport across a spike-like barrier decreases approximately as:

$$P_{transport} \propto \exp\left(-\frac{\Delta E_{spike}}{k_B T}\right) \tag{16}$$

where $\Delta E_{spike}$ is the positive conduction-band barrier. At room temperature, $k_BT$ is approximately 25.9 meV; therefore, a + 0.14 eV barrier corresponds to approximately 5.4 $k_BT$ and can substantially hinder electron extraction. This explains why excessive oxygen incorporation may degrade the fill factor and overall device performance despite improving buffer transparency.

In addition to the conduction-band offset, the valence-band offset is an important descriptor of carrier selectivity at the $Sb_2Se_3$/buffer heterointerface. Using the convention $\Delta E_v = E_{V,Sb_2Se_3} - E_{V,buffer}$, the valence-band offset can be expressed as:

$$\Delta E_v = (E_{g,buffer} - E_{g,Sb_2Se_3}) - \Delta E_c \tag{17}$$

For the optimized $In_2S_{2.685}O_{0.315}$ composition, $E_{g,buffer} = 2.70eV$, $E_{g,Sb_2Se_3} = 1.20eV$, and $\Delta E_c = -0.01eV$, giving: $\Delta E_v = (2.70 - 1.20) - (-0.01) = 1.51eV$.

This relatively large valence-band discontinuity provides an effective energetic barrier against hole transfer from the p-type $Sb_2Se_3$ absorber into the n-type buffer layer. Consequently, holes remain preferentially confined within the absorber and are directed toward the rear contact, whereas photogenerated electrons can be efficiently transferred toward the front contact through the nearly flat conduction-band alignment. This combination therefore improves carrier selectivity and reduces the probability of interfacial carrier loss. Interestingly, the adopted composition-dependent parameter set yields a VBO that progressively increases with increasing oxygen fraction. For $x = 1$, $\Delta E_v = (1.92 - 1.20) - (-0.26) = 0.98eV$, whereas for 1-x = 0.14, $\Delta E_v = (3.05 - 1.20) - (+0.14) = 1.71eV$. Thus, within the present parameterization, oxygen incorporation predominantly tunes the conduction-band edge of $In_2(O,S)_3$ while maintaining a substantial hole-blocking valence-band discontinuity across the investigated composition range. At the optimum 1-x = 0.105, the simultaneous occurrence of an almost flat CBO ($\Delta E_c \approx -0.01eV$) and a large VBO ($\Delta E_v \approx 1.51eV$) provides favorable asymmetric carrier selectivity at the $Sb_2Se_3/In_2(O,S)_3$ heterojunction.

It should nevertheless be emphasized that the band offsets discussed in this work are derived using an idealized electron-affinity-based heterojunction model. This approach assumes an abrupt interface and determines the band discontinuities from the adopted effective electron affinities and bandgaps of the interacting semiconductors. In experimentally fabricated $Sb_2Se_3/In_2(O,S)_3$ heterojunctions, the actual band alignment may additionally be influenced by interface dipoles and charge redistribution, Fermi-level pinning associated with interface defect states, chemical bonding or secondary-phase formation, elemental interdiffusion across the junction, and surface-termination-dependent electronic states. These phenomena can generate interface-specific potential shifts and consequently modify both the CBO and VBO relative to the values predicted from the ideal electron-affinity rule. Therefore, the calculated band offsets should be regarded as first-order design parameters within the present SCAPS-1D framework rather than exact experimentally guaranteed band discontinuities. Nevertheless, because the same band-alignment formalism is consistently applied to all investigated buffer compositions, the calculated trends remain useful for identifying the relative effect of oxygen incorporation on heterojunction energetics. Experimental interface-sensitive measurements will ultimately be required to determine the absolute band offsets of fabricated $Sb_2Se_3/In_2(O,S)_3$ interfaces and to verify the predicted near-flat conduction-band alignment.

The optical response also supports the benefit of controlled oxygen alloying. The absorption-coefficient spectra show that increasing the oxygen fraction shifts the absorption edge of $In_2(O,S)_3$ toward shorter wavelengths, consistent with band-gap widening. This reduces parasitic absorption in the front buffer layer and allows a larger fraction of high-energy photons to reach the $Sb_2Se_3$ absorber. Consequently, oxygen incorporation improves the short-wavelength spectral response while simultaneously enabling band-offset modulation. However, the optical and electronic effects must be optimized together: maximum oxygen content does not necessarily produce maximum device performance, because an excessive positive spike can compromise electron transport [26,45].

Therefore, the $In_2S_{2.685}O_{0.315}$ buffer layer with 1-x = 0.105 represents the most balanced composition among the studied cases. It combines improved optical transparency with an almost flat absorber/buffer conduction-band alignment, thereby minimizing interfacial recombination without introducing a significant extraction barrier. This optimized interfacial condition is expected to increase $V_{oc}$, maintain strong $J_{sc}$, enhance FF, and ultimately improve the power conversion efficiency of the Cd-free $Sb_2Se_3$ solar cell.

A parametric sweep in SCAPS-1D was used to evaluate how the oxygen fraction of the $In_2(O,S)_3$ buffer affects band alignment and device performance. The ratio 1-x was systematically varied from 0 to 0.14 while the remaining device parameters were maintained unchanged, allowing the corresponding changes in bandgap, effective electron affinity, conduction-band offset, carrier transport, and photovoltaic output to be directly correlated. On this basis, 1-x = 0.105 ($In_2S_{2.685}O_{0.315}$) represents the optimum condition: its bandgap of approximately 2.70 eV provides improved buffer transparency, while an effective electron affinity of approximately 4.05 eV produces an almost flat conduction-band offset of −0.01 eV with $Sb_2Se_3$. Lower oxygen contents retain detrimental cliff-like offsets, whereas higher oxygen fractions continue to widen the optical bandgap but introduce increasingly positive spike-like barriers. Thus, the optimum composition is determined by the simultaneous minimization of optical and recombination losses while maintaining efficient electron extraction, rather than by maximizing the oxygen concentration or buffer bandgap alone [57,58].

The composition-dependent results obtained in this study allow several general design principles to be established for buffer-layer engineering in $Sb_2Se_3$ thin-film solar cells. An effective buffer should first possess a sufficiently wide optical bandgap to minimize parasitic front-side absorption while maintaining favorable electronic coupling with the absorber. More critically, its electron affinity should be selected to produce a nearly flat or moderately positive conduction-band offset at the $Sb_2Se_3$/buffer interface. A pronounced negative cliff enhances interfacial recombination and limits the quasi-Fermi-level splitting and $V_{oc}$, whereas an excessively large positive spike hinders electron extraction and decreases the fill factor. Buffer optimization must therefore balance optical transparency, recombination suppression, and carrier transport rather than maximizing any individual material parameter. In addition, favorable junction electrostatics, low interfacial charge accumulation, and high recombination resistance are desirable

because they promote carrier separation and selective extraction. Within this framework, the optimum composition corresponds to the condition at which the buffer provides sufficient optical transparency while its electron affinity closely matches that required for favorable $Sb_2Se_3$ heterojunction energetics. For the present $In_2(O_{1-x},S_x)_3$ system, this balance is achieved at 1-x = 0.105, where $E_g \approx 2.70$ eV, $\chi \approx 4.05$ eV, and $\Delta E_c \approx -0.01$ eV. These criteria provide a broader design guideline for evaluating other composition-engineered Cd-free buffer materials for $Sb_2Se_3$ photovoltaics.

Fig. 3 provides a direct visualization of the band-edge evolution induced by composition engineering of the $In_2(O_{1-x},S_x)_3$ buffer layer. The progressive reduction in the adopted effective electron affinity with increasing oxygen fraction raises the buffer conduction-band edge relative to that of $Sb_2Se_3$, thereby continuously modifying the interfacial transport landscape. In the S-rich limit, the resulting $\Delta E_c$ of approximately −0.26 eV forms a pronounced cliff, which energetically favors electron accumulation near the junction and increases the probability of interfacial SRH recombination. As the oxygen fraction is increased, this unfavorable discontinuity is progressively relaxed, with $\Delta E_c$ approaching zero and the interface evolving toward a quasi-flat conduction-band configuration.

A particularly favorable alignment is obtained at x = 0.895, corresponding to an oxygen fraction of 1-x = 0.105 and the nominal composition $In_2S_{2.685}O_{0.315}$. At this condition, $\Delta E_c \approx -0.01$ eV, indicating that the conduction bands are nearly aligned. Such a configuration is advantageous because it removes most of the recombination-promoting cliff while avoiding the formation of an appreciable barrier to majority-electron transfer. The electronic significance of this point is therefore not simply that the CBO approaches zero, but that the interface simultaneously favors carrier selectivity, reduced recombination current, and efficient electron collection.

Beyond this composition, further oxygen incorporation drives $\Delta E_c$ into the positive regime, reaching approximately + 0.06 eV and + 0.14 eV at oxygen fractions of 0.12 and 0.14, respectively. The emergence of a moderate positive offset can still improve interfacial selectivity by opposing minority-carrier recombination; however, as the spike becomes larger, the energetic cost of electron transfer across the junction also increases. Consequently, the band-alignment evolution shown in Fig. 3 identifies a narrow energetic window between recombination-dominated cliff behavior and transport-limited spike behavior. The optimum composition is located within this window, where the heterointerface provides the most favorable compromise between recombination suppression and electron-extraction efficiency.

Fig. 4(a),(b) illustrates the composition-dependent optical response of the $In_2(O_{1-x},S_x)_3$ buffer layer. As the oxygen fraction, 1 −x = O/(O+S), increases from 0 to 0.14, the adopted bandgap increases from 1.92 to 3.05 eV, resulting in a progressive shift of the absorption edge toward shorter wavelength. The wavelength-dependent absorption-coefficient spectra, $\alpha(\lambda)$, therefore indicate reduced parasitic absorption in the front buffer over an increasingly larger portion of the incident solar spectrum. This enhanced transparency allows a greater fraction of short-wavelength photons to reach the $Sb_2Se_3$ absorber and can contribute to improved carrier photogeneration. Importantly, the optical benefit of increasing oxygen content must be considered together with the corresponding evolution of the electronic band alignment. Although higher oxygen fractions improve buffer transparency, excessive oxygen incorporation drives the conduction-band offset into a positive spike regime, which can hinder electron extraction. Consequently, the optimum composition does not correspond to the maximum bandgap or oxygen content, but rather to a balance between reduced optical losses and favorable interfacial carrier transport. This balance is achieved near x = 0.895 (1-x = 0.105), corresponding to $In_2S_{2.685}O_{0.315}$.

### 3.3. Photovoltaic performance optimization through oxygen-alloyed $In_2(O,S)_3$ buffer layers

The effect of oxygen incorporation in the $In_2(O,S)_3$ buffer layer on the photovoltaic output of $Sb_2Se_3$ solar cells were evaluated using the calibrated SCAPS-1D model. Fig. 5 displays the simulated J-V characteristics for devices with different oxygen-to-anion ratios, and the corresponding photovoltaic parameters are summarized in Table 3. The results reveal a strongly composition-dependent device response, in which $V_{oc}$, FF, and PCE vary significantly with oxygen content, whereas $J_{sc}$ remains nearly invariant. This indicates that the dominant role of oxygen alloying is not to increase the total photogenerated current, but to modify junction energetics, recombination kinetics, and carrier extraction across the $Sb_2Se_3/In_2(O,S)_3$ interface.

For the pure $In_2S_3$ buffer layer, corresponding to x = 1, the device yields $V_{oc}$= 0.377 V, $J_{sc}$= 34.192 $mA\,cm^{-2}$, FF= 61.271%, and PCE= 7.899%. Although the photocurrent is already high, the relatively poor $V_{oc}$ and FF indicate that the device is limited by non-radiative recombination and non-ideal interfacial transport rather than by

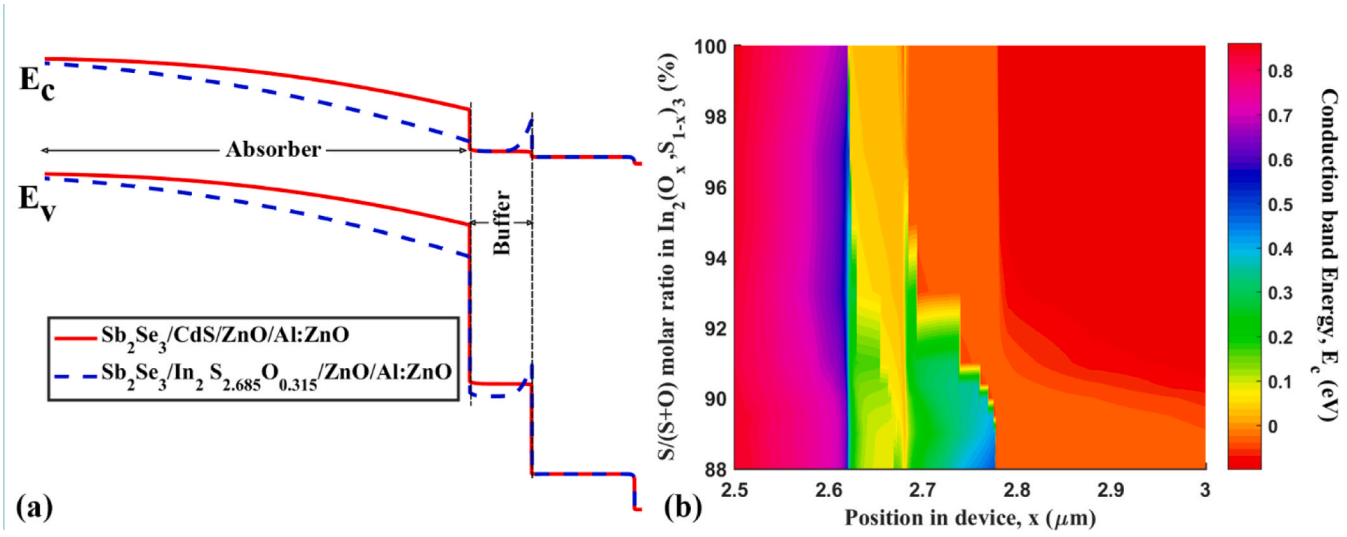


**Fig. 3.** Band-alignment engineering at the $Sb_2Se_3$/buffer interface through oxygen-alloyed $In_2(O,S)_3$. (a) Equilibrium energy-band diagrams of the conventional $Sb_2Se_3$/CdS/ZnO/Al structure and the optimized $Sb_2Se_3/In_2S_{2.685}O_{0.315}$/ZnO/Al structure. (b) Composition-dependent conduction-band energy distribution as a function of position and oxygen-to-anion ratio in the $In_2(O_{1-x},S_x)_3$ buffer layer. Oxygen incorporation progressively changes the absorber/buffer interface from cliff-like alignment toward a nearly flat and then spike-like configuration.

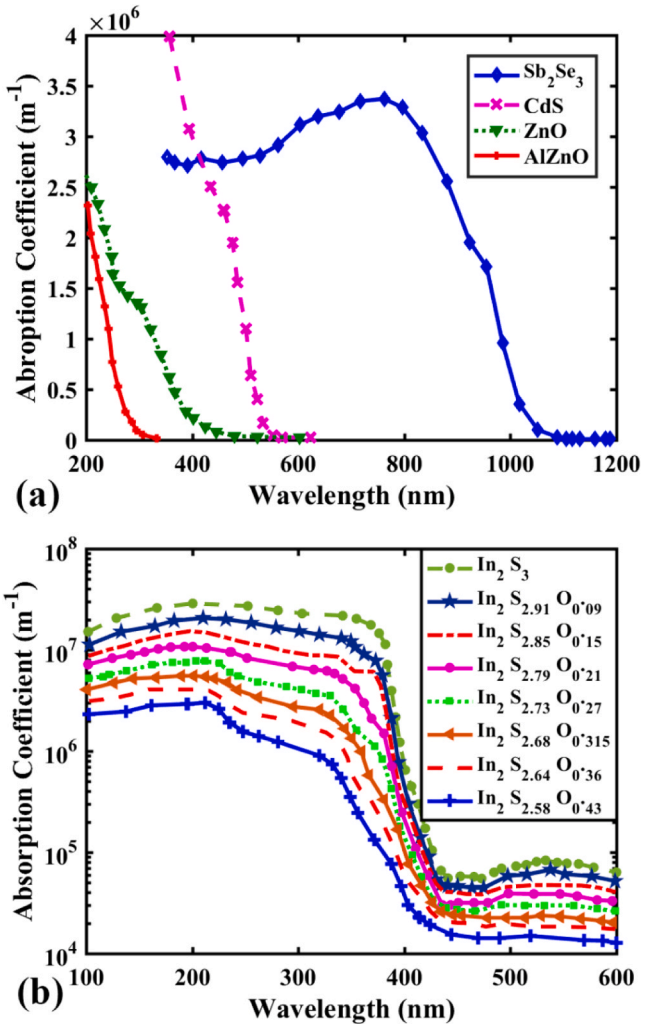


**Fig. 4.** Optical absorption characteristics of the materials used in the simulated solar-cell structures. (a) Absorption-coefficient spectra of $Sb_2Se_3$, CdS, ZnO, and Al layers. (b) Composition-dependent wavelength-resolved absorption-coefficient spectra of $In_2(O_{1-x},S_x)_3$ buffer layers. The optical profiles are anchored to experimentally reported absorption spectra of β-$In_2S_{3-3x}O_{3x}$ thin films, with intermediate simulated compositions obtained by composition interpolation. The progressive displacement of the absorption edge with oxygen incorporation reduces front-side parasitic absorption.

insufficient optical generation. At open circuit, the photogenerated current is balanced by the recombination current, which can be expressed as:

$$J_{rec} = q\int R(x)dx \tag{18}$$

where $J_{rec}$ is the recombination current density and R(x) is the position-dependent recombination rate. A large cliff-like offset at the $Sb_2Se_3$/$In_2S_3$ interface increases R(x) near the heterojunction, thereby increasing $J_{rec}$ and reducing the achievable quasi-Fermi-level splitting. Since the open-circuit voltage is directly linked to this splitting,

$$qV_{oc} \approx E_{F_n} - E_{F_p} \tag{19}$$

where $E_{F_n}$ and $E_{F_p}$ are the electron and hole quasi-Fermi levels, respectively, the low $V_{oc}$ of the pure $In_2S_3$-based device can be attributed to enhanced interface-assisted recombination.

With increasing oxygen content, the photovoltaic performance improves progressively. When 1-x increases from 0 to 0.03, $V_{oc}$ rises from 0.377 to 0.461 V and the PCE increases from 7.899% to 10.256%.

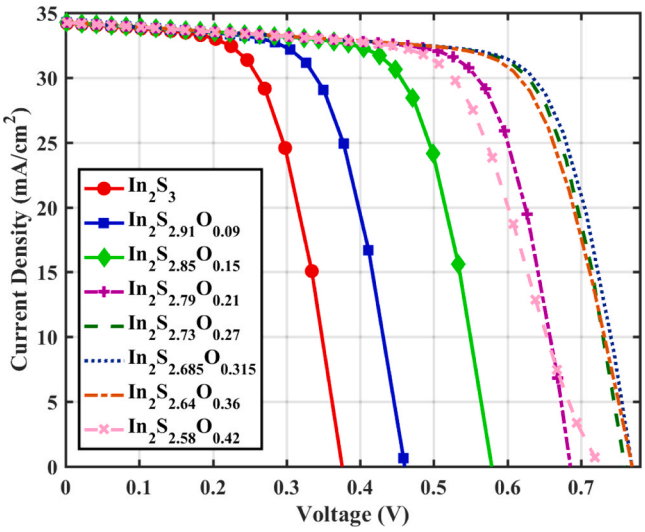


**Fig. 5.** Simulated current-voltage characteristics of $Sb_2Se_3$ solar cells employing $In_2(O,S)_3$ buffer layers with different oxygen-to-anion ratios. The progressive improvement in $V_{oc}$ and FF with increasing oxygen content up to the optimized composition reflects the suppression of cliff-induced interfacial recombination, whereas excessive oxygen incorporation leads to a spike-like extraction barrier and degraded device performance.

**Table 3**
Simulated photovoltaic performance of $Sb_2Se_3$ thin-film solar cells using $In_2(O,S)_3$ buffer layers with different oxygen ratios. The physical parameters corresponding to each x value are listed in Table 2.

| Approximate composition | $V_{oc}$ (V) | $J_{sc}$ ($mA/cm^2$) | FF (%) | PCE, η (%) | Δη (percentage points) relative to (1 −x) = 0 |
|---|---|---|---|---|---|
| $In_2S_3$ | 0.377 | 34.192 | 61.271 | 7.899 | 0.000 |
| $In_2S_{2.91}O_{0.09}$ | 0.461 | 34.232 | 65.039 | 10.256 | + 2.357 |
| $In_2S_{2.85}O_{0.15}$ | 0.579 | 34.250 | 69.136 | 13.716 | + 5.817 |
| $In_2S_{2.79}O_{0.21}$ | 0.687 | 34.255 | 71.543 | 16.848 | + 8.949 |
| $In_2S_{2.73}O_{0.27}$ | 0.760 | 34.240 | 72.674 | 18.907 | + 11.008 |
| **$In_2S_{2.685}O_{0.315}$** | **0.771** | **34.250** | **72.432** | **19.123** | **+ 11.224** |
| $In_2S_{2.64}O_{0.36}$ | 0.770 | 34.253 | 70.341 | 18.546 | + 10.647 |
| $In_2S_{2.58}O_{0.42}$ | 0.727 | 34.242 | 63.498 | 15.814 | + 7.916 |

Further increasing 1-x to 0.05 and 0.07 enhances the PCE to 13.716% and 16.848%, respectively. This continuous improvement demonstrates that moderate oxygen incorporation reduces the recombination activity of the absorber/buffer interface by alleviating the detrimental cliff-like band alignment. As a result, the recombination current decreases, the quasi-Fermi-level splitting increases, and the J-V curves shift toward higher output voltage.

The optimum photovoltaic response is obtained for the $In_2S_{2.685}O_{0.315}$ buffer layer, corresponding to 1-x = 0.105. At this composition, the device achieves $V_{oc}$= 0.771 V, $J_{sc}$= 34.250 $mA\ cm^{-2}$, FF= 72.432%, and PCE= 19.123%. Compared with the pure $In_2S_3$-buffered device, this represents an absolute efficiency gain of 11.224 % age points. The enhancement is mainly driven by the large increase in $V_{oc}$ and FF, while $J_{sc}$ changes only marginally. This can be understood from the efficiency relation:

$$\eta = \frac{V_{oc} \times J_{sc} \times FF}{P_{in}} \tag{20}$$

For small relative changes, the efficiency variation can be approximated as:

$$\frac{\Delta\eta}{\eta} \approx \frac{\Delta V_{oc}}{V_{oc}} + \frac{\Delta J_{sc}}{J_{sc}} + \frac{\Delta FF}{FF} \quad (21)$$

This relation shows that the efficiency enhancement is dominated by the voltage and fill-factor terms. In the present case, the nearly unchanged $J_{sc}$ confirms that oxygen alloying primarily improves the electrical quality of the heterojunction rather than the optical generation capacity of the absorber.

The improvement in FF also provides important information about carrier extraction and diode quality. The fill factor is defined as:

$$FF = \frac{(V_m \times J_m)}{(V_{oc} \times J_{sc})} \quad (22)$$

where $V_m$ and $J_m$ are the voltage and current density at the maximum power point. A higher FF indicates that the device can maintain a larger fraction of its ideal rectangular J-V response under operating conditions. The increase in FF from 61.271% for x = 1–72.432% for 1-x = 0.105 therefore suggests reduced recombination loss, improved carrier selectivity, and more efficient electron transport across the $Sb_2Se_3/In_2(O,S)_3$ interface.

However, the performance does not improve monotonically with oxygen content. When 1-x exceeds the optimum value, the conduction-band offset becomes increasingly positive and the interface evolves into a more pronounced spike-like configuration. At 1-x = 0.12, the device still delivers a high PCE of 18.546%, but the FF decreases to 70.341%. At 1-x = 0.14, the degradation becomes more evident, with $V_{oc}$ decreasing to 0.727 V, FF dropping to 63.498%, and PCE falling to 15.814%. This decline indicates that excessive oxygen incorporation creates an electron-extraction barrier at the absorber/buffer interface. Under this condition, photogenerated electrons can accumulate near the junction, increasing transport resistance and reducing the maximum power output.

The evolution of the J-V curves in Fig. 5 clearly reflects this balance between recombination suppression and transport limitation. Up to 1-x = 0.105, the curves shift toward higher voltage and improved rectangularity, indicating enhanced junction quality and reduced recombination loss. Beyond this composition, the curves become less ideal because the increasingly positive barrier restricts electron extraction and lowers the fill factor. Therefore, the optimum buffer composition is not determined by the widest bandgap or the highest oxygen content, but by the condition that simultaneously minimizes interfacial recombination and preserves barrier-free carrier transport.

Generally, the composition-dependent photovoltaic analysis confirms that oxygen-alloyed $In_2(O,S)_3$ is an effective functional buffer layer for Cd-free $Sb_2Se_3$ solar cells. The optimized $In_2S_{2.685}O_{0.315}$ composition provides the best compromise between optical transparency, interfacial band alignment, recombination suppression, and electron extraction. The resulting improvement from 7.899% to 19.123% demonstrates that precise buffer-layer alloying can transform $In_2(O,S)_3$ from a simple Cd-free replacement into a performance-enabling interfacial layer for high-efficiency $Sb_2Se_3$ thin-film photovoltaics.

Fig. 6 reveals a distinctly non-monotonic photovoltaic response to oxygen incorporation, indicating that the optimum buffer composition is governed by competing interfacial and transport effects rather than by a simple monotonic improvement in any single material property. The most pronounced composition sensitivity is observed in $V_{oc}$, which rises substantially as the oxygen fraction increases toward 1-x = 0.105. This behavior is consistent with the progressive relaxation of the negative

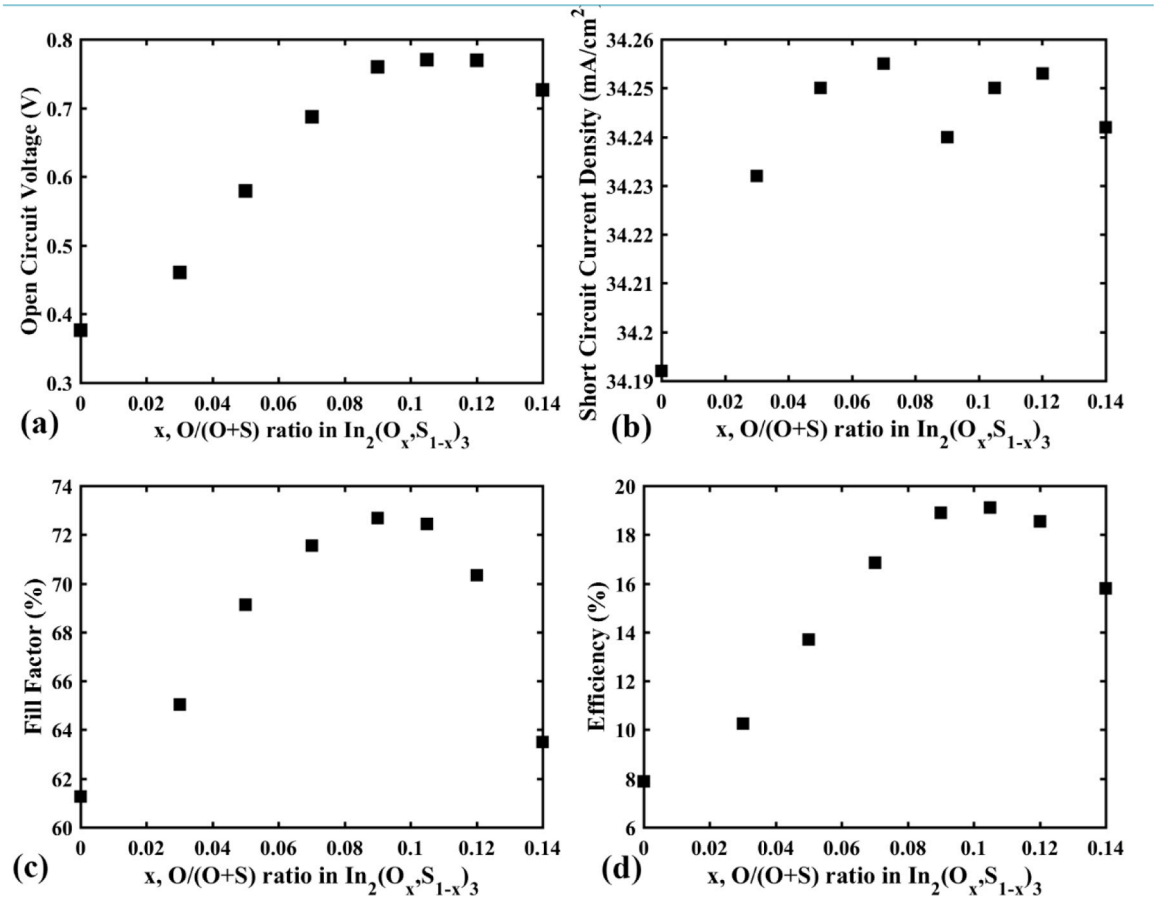


**Fig. 6.** Composition-dependent photovoltaic parameters of $Sb_2Se_3/In_2(O_{1-x},S_x)_3$ solar cells as a function of oxygen-to-anion ratio. (a) Open-circuit voltage, (b) short-circuit current density, (c) fill factor, and (d) power conversion efficiency. The optimum performance is obtained near 1-x = 0.105, where the $In_2S_{2.685}O_{0.315}$ buffer layer provides a nearly flat conduction-band alignment with $Sb_2Se_3$.

conduction-band discontinuity and the associated reduction in heterojunction recombination losses. By contrast, $J_{sc}$ exhibits only a weak dependence on composition over most of the investigated range, indicating that the efficiency gain is not primarily driven by enhanced photogeneration, but instead by improved carrier selectivity and reduced voltage loss at the absorber/buffer interface.

The evolution of FF further clarifies the existence of a narrow optimum energetic window. As the cliff-like offset is progressively suppressed, improved interfacial transport and reduced recombination losses enhance the device fill factor. Once the conduction-band offset becomes appreciably positive, however, the interface begins to impose an increasing energetic penalty on electron transfer, leading to a deterioration in FF despite the continued widening of the buffer bandgap. The resulting PCE maximum at 1-x = 0.105 (x = 0.895), corresponding to $In_2S_{2.685}O_{0.315}$, therefore reflects the point at which recombination suppression and electron-extraction efficiency are most favorably balanced. At this composition, $\Delta E_c \approx -0.01$ eV places the heterojunction close to the transition between cliff- and spike-dominated transport, allowing the device to benefit from reduced interfacial losses without introducing a significant extraction barrier. The decline in performance beyond this point demonstrates that further optical-gap widening alone is insufficient to improve device efficiency when accompanied by increasingly unfavorable transport energetics. Thus, Fig. 6 identifies interfacial band-edge matching, rather than maximum oxygen incorporation, as the dominant criterion governing the optimum photovoltaic response.

### 3.4. Comparative analysis of the optimized Cd-free device and the conventional CdS-based reference cell

To evaluate the practical relevance of the optimized buffer design, the best-performing Cd-free device was directly benchmarked against the conventional CdS-based reference cell. The optimized structure employs $In_2S_{2.685}O_{0.315}$ as the buffer layer, corresponding to 1-x = 0.105, where the $Sb_2Se_3$/buffer interface approaches an almost flat conduction-band configuration. This comparison is essential because it distinguishes a merely Cd-free replacement from a genuinely performance-enhancing interfacial modification.

Fig. 7 compares the simulated J-V characteristics of the conventional Mo/$MoSe_2$/$Sb_2Se_3$/CdS/ZnO/Al:ZnO reference cell and the optimized Mo/$MoSe_2$/$Sb_2Se_3$/$In_2S_{2.685}O_{0.315}$/ZnO/Al:ZnO device. The CdS-based reference cell delivers $V_{oc}$= 0.480 V, $J_{sc}$= 30.87 $mA\ cm^{-2}$, FF= 67.18%, and PCE= 10.12%. After replacing CdS with the optimized $In_2S_{2.685}O_{0.315}$ buffer, the device output increases to $V_{oc}$= 0.771 V, $J_{sc}$= 34.25 $mA\ cm^{-2}$, FF= 72.43%, and PCE= 19.12%. The absolute efficiency gain is therefore 9.00 %age points, while the relative efficiency enhancement is given by:

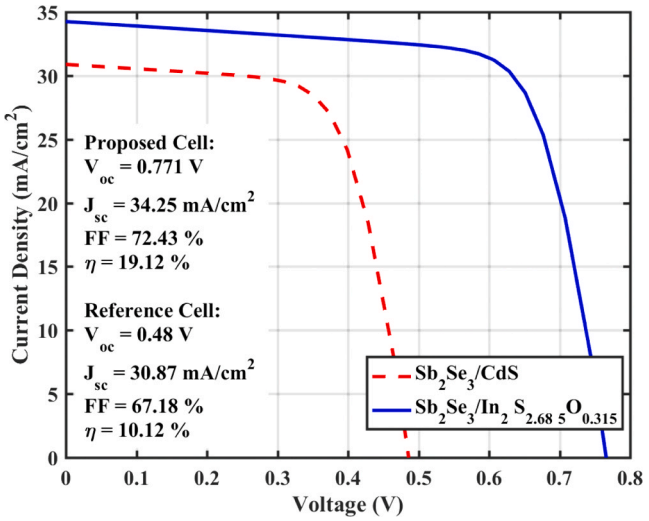


**Fig. 7.** Direct comparison of the simulated current-voltage characteristics of the conventional $Sb_2Se_3$/CdS reference cell and the optimized Cd-free $Sb_2Se_3$/$In_2S_{2.685}O_{0.315}$ device. Replacing CdS with the optimized oxygen-alloyed $In_2(O,S)_3$ buffer substantially improves $V_{oc}$, $J_{sc}$, FF, and PCE, demonstrating the combined benefits of reduced optical loss, improved carrier selectivity, and suppressed interfacial recombination.

$$Relative\ PCE\ gain = \left[\frac{(\eta_{opt} - \eta_{ref})}{\eta_{ref}}\right] \times 100 \quad (23)$$

Using the simulated efficiencies, the optimized Cd-free device exhibits an approximate relative improvement of 89% compared with the CdS-based reference cell. This substantial increase confirms that the $In_2S_{2.685}O_{0.315}$ layer does not simply replace CdS from an environmental perspective, but actively improves the junction quality and photovoltaic output [59].

The most significant contribution arises from the increase in $V_{oc}$ from 0.480 to 0.771 V. This enhancement indicates a pronounced reduction in non-radiative recombination at the absorber/buffer interface. In the CdS-based device, imperfect interfacial energetics and recombination-active states limit the quasi-Fermi-level splitting under illumination. In contrast, the optimized $In_2S_{2.685}O_{0.315}$ buffer reduces the recombination-active cliff condition while preserving efficient electron extraction. As a result, the optimized device sustains a larger internal photovoltage and exhibits a substantially improved open-circuit voltage.

The large enhancement in ($V_{oc}$) requires consideration of both recombination losses and quasi-Fermi-level splitting. In the present comparison, the $Sb_2Se_3$ absorber properties and bulk-defect parameters were maintained unchanged; therefore, the composition-dependent increase in ($V_{oc}$) cannot be attributed to an imposed reduction in the absorber bulk-defect density. Instead, the dominant modification occurs at the absorber/buffer heterointerface. Although the interface-state density and carrier-capture parameters are maintained consistently, the interface recombination rate remains sensitive to the local electron and hole populations, which are strongly affected by the conduction-band offset. The nearly flat ($\Delta E_c \approx -0.01$ eV) obtained for $In_2S_{2.685}O_{0.315}$ reduces minority-carrier accumulation near the heterojunction and consequently lowers the probability of SRH-assisted interfacial recombination. The resulting reduction in recombination current allows a larger separation of the electron and hole quasi-Fermi levels under illumination and therefore a higher open-circuit voltage. Quantitatively, using the $Sb_2Se_3$ bandgap of 1.20 eV employed in the present model, the voltage deficit ($E_g/q - V_{oc}$) decreases from approximately 0.720 V for the CdS reference device to 0.429 V for the optimized device, corresponding to a recovery of approximately 0.291 V in photovoltage. This reduction in voltage deficit, together with the increased recombination resistance and stronger built-in potential obtained for the optimized structure, supports the interpretation that suppression of heterointerfacial recombination is the principal origin of the observed increase in ($V_{oc}$).

The increase in $J_{sc}$ from 30.87 to 34.25 $mA\ cm^{-2}$ further indicates that the optimized Cd-free buffer improves the spectral harvesting and carrier-collection capability of the device. This improvement originates from the combined effect of reduced parasitic absorption in the front buffer region and enhanced charge collection at the $Sb_2Se_3$/buffer interface. Compared with CdS, the oxygen-alloyed $In_2(O,S)_3$ buffer possesses higher optical transparency in the short-wavelength region, allowing a larger fraction of high-energy photons to reach the $Sb_2Se_3$ absorber. At the same time, the more favorable interfacial band alignment improves the extraction probability of photogenerated electrons near the junction.

The spectral origin of the photocurrent enhancement is examined in Fig. 8 using the differential external quantum efficiency:

$$\Delta EQE(\lambda) = EQE_{opt}(\lambda) - EQE_{ref}(\lambda) \quad (24)$$

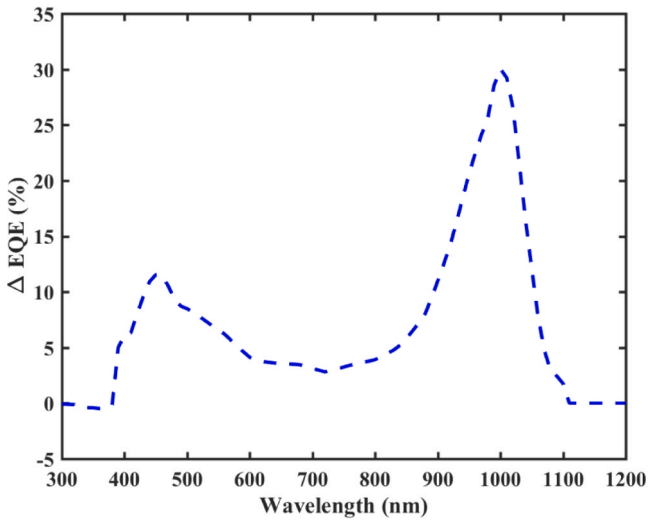


**Fig. 8.** Differential external quantum efficiency between the optimized Cd-free $Sb_2Se_3/In_2S_{2.685}O_{0.315}$ device and the conventional $Sb_2Se_3$/CdS reference cell. The positive ΔEQE over a broad spectral range confirms the enhanced wavelength-dependent carrier generation and collection enabled by the optimized buffer layer, particularly through reduced front-side parasitic absorption and improved absorber/buffer interface quality.

where $EQE_{opt}(\lambda)$ is the spectral response of the optimized $In_2S_{2.685}O_{0.315}$-buffered device and $EQE_{ref}(\lambda)$ is that of the CdS-based reference cell. The corresponding photocurrent gain associated with the EQE enhancement can be expressed as:

$$\Delta J_{sc,EQE} = q \int \Phi_{AM1.5} G(\lambda)\, \Delta EQE(\lambda) \quad d\lambda \tag{25}$$

where $\Phi_{AM1.5}G(\lambda)$ is the incident photon flux under AM1.5 G illumination. The positive $\Delta EQE$ over a broad wavelength range confirms that the optimized buffer increases the number of photons effectively converted into collected carriers. The enhancement in the short-wavelength region is mainly attributed to the reduced front-side absorption loss after replacing CdS, whereas improvement at longer wavelengths reflects more efficient carrier collection inside the $Sb_2Se_3$ absorber due to reduced recombination and improved junction electrostatics.

The fill factor also increases from 67.18% to 72.43%, indicating improved diode quality and reduced transport-related losses. This improvement is consistent with a more favorable balance between recombination suppression and electron extraction at the optimized interface. In the CdS-based structure, interfacial recombination and non-ideal carrier selectivity distort the J-V curve and reduce the maximum power point. By contrast, the $In_2S_{2.685}O_{0.315}$ buffered device exhibits a more rectangular J-V response, reflecting lower recombination current, improved charge selectivity, and more efficient carrier transport across the heterojunction.

The replacement of CdS by composition-engineered $In_2(O_{1-x},S_x)_3$ therefore affects the device through two coupled mechanisms rather than through a simple material substitution. Optically, the wider-bandgap oxygen-alloyed buffer reduces parasitic front-side absorption and increases the photon flux reaching the $Sb_2Se_3$ absorber. Electronically, control of the oxygen fraction shifts the conduction-band offset toward an almost flat configuration, thereby suppressing interface-assisted recombination without introducing a significant barrier to electron extraction. These effects collectively account for the simultaneous enhancement of $V_{oc}$, $J_{sc}$, FF, and PCE observed for the optimized Cd-free device. The comparison further demonstrates that the principal advantage of $In_2(O_{1-x},S_x)_3$ lies in its compositional tunability, which allows optical transparency and heterojunction energetics to be optimized concurrently [60].

These results demonstrate that the replacement of CdS by composition-engineered $In_2(O,S)_3$ provides benefits beyond the elimination of a Cd-containing component. The optimized $In_2S_{2.685}O_{0.315}$ buffer simultaneously increases optical transparency and improves the electronic quality of the $Sb_2Se_3$/buffer heterojunction. Its wider bandgap reduces parasitic front-side absorption, whereas its composition-tuned electron affinity produces an almost flat conduction-band offset that suppresses interface-assisted recombination without significantly hindering electron extraction. Consequently, all major photovoltaic parameters improve simultaneously relative to the CdS-based reference device. Within the calibrated SCAPS-1D framework, the resulting increase in PCE from 10.12% to 19.12% indicates that Cd elimination does not necessarily require a performance compromise; instead, appropriate Cd-free buffer engineering can provide both environmental and photovoltaic advantages. However, the predicted absolute efficiency should be regarded as a simulation-guided target that requires experimental validation of the optimum $In_2(O,S)_3$ composition and interface properties.

As a whole, the direct comparison demonstrates that the optimized $In_2S_{2.685}O_{0.315}$ buffer layer simultaneously improves all key photovoltaic parameters relative to the CdS reference device. The performance enhancement is not governed by a single factor, but by the coupled reduction of parasitic optical absorption, mitigation of interfacial recombination, improvement of carrier selectivity, and enhancement of charge collection. These results establish oxygen-alloyed $In_2(O,S)_3$ as a highly effective Cd-free buffer platform for high-performance $Sb_2Se_3$ thin-film solar cells.

### 3.5. Charge-storage behavior, built-in potential, and impedance analysis

To clarify the physical mechanisms responsible for the superior performance of the optimized Cd-free device, capacitance-frequency, Mott-Schottky, and impedance analyses were carried out for the conventional $Sb_2Se_3$/CdS reference cell and the optimized $Sb_2Se_3/In_2S_{2.685}O_{0.315}$ device. These diagnostic analyses are particularly important because they provide information beyond the J-V response, allowing the effects of buffer-layer engineering on charge accumulation, depletion-region electrostatics, built-in potential, and recombination resistance to be evaluated more directly.

Fig. 9 shows the capacitance-frequency response of the reference and optimized devices. The $Sb_2Se_3$/CdS cell exhibits a higher capacitance

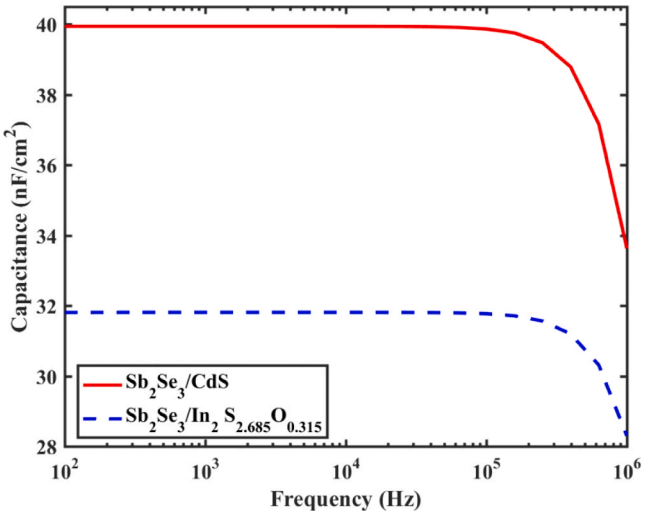


**Fig. 9.** Capacitance-frequency response of the conventional $Sb_2Se_3$/CdS reference cell and the optimized $Sb_2Se_3/In_2S_{2.685}O_{0.315}$ device. The lower capacitance of the optimized Cd-free device indicates reduced interfacial charge accumulation, weaker trap-assisted polarization, and improved depletion-region behavior at the absorber/buffer junction.

over the investigated frequency range, with a low-frequency value of approximately 40 $nF\ cm^{-2}$. In contrast, the optimized $In_2S_{2.685}O_{0.315}$-buffered device shows a lower capacitance of approximately 32 $nF\ cm^{-2}$. Since low-frequency capacitance is sensitive to slowly responding defect states, interfacial polarization, and carrier trapping, the lower capacitance of the optimized device indicates weaker charge storage at the absorber/buffer interface. This result suggests that oxygen-alloyed $In_2(O,S)_3$ reduces electrically active interfacial response and suppresses charge accumulation near the heterojunction.

The area-normalized capacitance is related to the depletion width by:

$$C_A = \frac{\varepsilon\varepsilon_0}{W} \tag{26}$$

where $C_A$ is the capacitance per unit area, $\varepsilon$ is the relative dielectric constant, $\varepsilon_0$ is the vacuum permittivity, and W is the depletion width. Accordingly, a lower capacitance corresponds to a wider or more effectively depleted space-charge region. The reduced capacitance of the optimized device therefore implies that the built-in electric field extends more efficiently across the junction, improving carrier separation and reducing the probability of recombination before charge collection.

The frequency dispersion of capacitance further reflects the response of trap states. In general, slow traps can follow the AC perturbation at low frequencies and contribute to the measured capacitance, whereas they cannot respond efficiently at higher frequencies. This behavior can be described qualitatively as:

$$C(\omega) = C_\infty + \frac{\Delta C}{\left[1 + (\omega\tau)^2\right]} \tag{27}$$

where $C(\omega)$ is the frequency-dependent capacitance, $C_\infty$ is the high-frequency capacitance, $\Delta C$ is the trap-related capacitance contribution, $\omega$ is the angular frequency, and $\tau$ is the characteristic trap response time. A smaller low-frequency capacitance contribution in the optimized device indicates a reduced trap-assisted capacitive response, confirming that the nearly flat $Sb_2Se_3/In_2S_{2.685}O_{0.315}$ band alignment suppresses interfacial charge accumulation and improves carrier selectivity.

Fig. 10 presents the Mott-Schottky plots, expressed as $1/C^2$ versus applied voltage. The built-in potential, $V_{bi}$, was extracted from the voltage-axis intercept of the linear region. The CdS-based reference device exhibits $V_{bi}$= 0.78 V, whereas the optimized Cd-free device shows a higher $V_{bi}$= 1.00 V. This increase indicates a stronger internal electrostatic field in the optimized heterojunction, which is beneficial for separating photogenerated electron-hole pairs and reducing recombination losses.

For an abrupt depletion approximation, the Mott-Schottky relation can be written as:

$$\frac{1}{C_A^2} = \frac{2(V_{bi} - V)}{q\varepsilon\varepsilon_0 N_{eff}} \tag{28}$$

where $C_A$ is the capacitance per unit area, $V_{bi}$ is the built-in potential, V is the applied voltage, q is the elementary charge, $\varepsilon\varepsilon_0$ is the absolute permittivity, and $N_{eff}$ is the effective doping concentration. The corresponding depletion width is:

$$W = \left[\frac{2\varepsilon\varepsilon_0(V_{bi} - V)}{qN_{eff}}\right]^{1/2} \tag{29}$$

These relations show that a higher $V_{bi}$ strengthens the junction field and increases the electrostatic driving force for carrier separation. Therefore, the increase of $V_{bi}$ from 0.78 to 1.00 V provides strong evidence that the optimized $In_2S_{2.685}O_{0.315}$ buffer improves the electrostatic quality of the $Sb_2Se_3$ heterojunction. This result is consistent with the higher $V_{oc}$ and improved FF obtained from the J-V characteristics.

The impedance spectra in Fig. 11 provide further evidence for improved recombination resistance in the optimized device. Both devices display semicircular Nyquist responses, which are characteristic of charge-transfer and recombination processes in thin-film solar cells. The optimized $Sb_2Se_3/In_2S_{2.685}O_{0.315}$ device exhibits a larger semicircle diameter than the $Sb_2Se_3$/CdS reference cell, indicating a higher resistance against recombination-mediated charge loss. This confirms that the optimized buffer layer suppresses interfacial recombination and improves charge-transfer selectivity at the absorber/buffer junction.

The impedance response can be interpreted using a simplified recombination-related equivalent circuit:

$$Z(\omega) = R_s + \frac{R_{rec}}{\left[1 + j\omega R_{rec} C_\mu\right]} \tag{30}$$

where $Z(\omega)$ is the frequency-dependent impedance, $R_s$ is the series resistance, $R_{rec}$ is the recombination resistance, $C_\mu$ is the chemical or

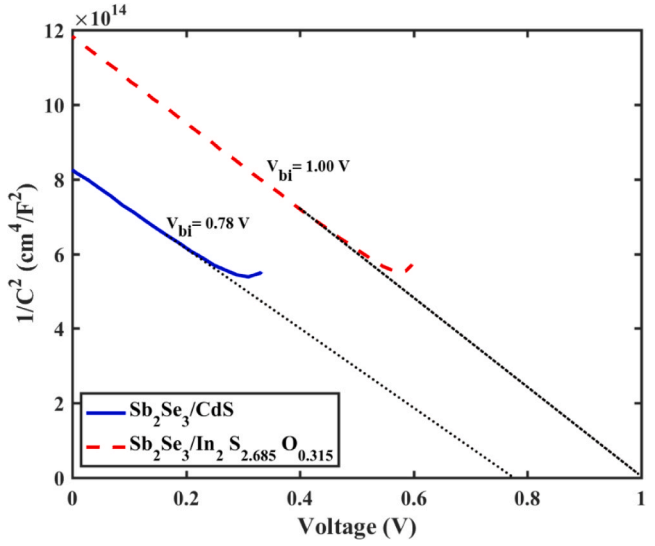


**Fig. 10.** Mott-Schottky analysis of the conventional $Sb_2Se_3$/CdS reference cell and the optimized $Sb_2Se_3/In_2S_{2.685}O_{0.315}$ device, plotted as $1/C^2$ versus applied voltage. The extracted built-in potential increases from 0.78 V for the CdS-based reference device to 1.00 V for the optimized Cd-free device, confirming the formation of a stronger internal electric field and more efficient charge separation.

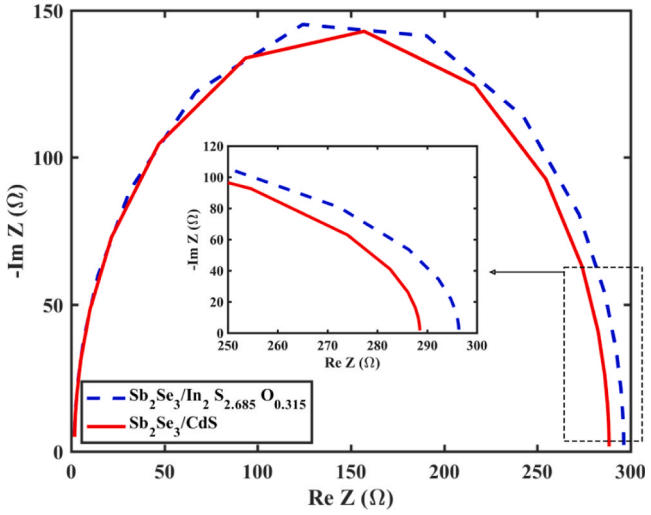


**Fig. 11.** Nyquist impedance spectra of the conventional $Sb_2Se_3$/CdS reference cell and the optimized $Sb_2Se_3/In_2S_{2.685}O_{0.315}$ device. The larger semicircle diameter observed for the optimized Cd-free device indicates enhanced recombination resistance and suppressed interfacial charge-transfer losses, consistent with the improved $V_{oc}$, FF, and power conversion efficiency.

junction capacitance, $\omega$ is the angular frequency, and j is the imaginary unit. In this model, the characteristic recombination lifetime is given by:

$$\tau_{rec} = R_{rec}\, C_{\mu} \tag{31}$$

A larger $R_{rec}$ therefore corresponds to slower recombination kinetics and longer effective carrier lifetime. The larger Nyquist semicircle observed for the optimized Cd-free device indicates that electrons and holes are less likely to recombine at the junction, which directly supports the enhanced $V_{oc}$ and FF [61].

Taken together, the capacitance and impedance results demonstrate that the performance enhancement of the optimized Cd-free device originates from improved junction physics rather than from a simple numerical increase in output parameters. The lower capacitance indicates suppressed interfacial charge storage and weaker trap-assisted polarization. The higher built-in potential confirms stronger internal electric-field formation and more efficient photocarrier separation. The larger recombination resistance reveals slower recombination kinetics and improved interfacial charge selectivity. These findings provide consistent physical evidence that the $In_2S_{2.685}O_{0.315}$ buffer layer simultaneously improves electrostatic field distribution, reduces charge accumulation, and suppresses recombination losses, leading to the enhanced $V_{oc}$, FF, and PCE of the optimized Cd-free $Sb_2Se_3$ solar cell.

### 3.6. Benchmarking against reported experimental $Sb_2Se_3$ solar cells

To place the optimized Cd-free device in a broader performance context, Table 4 compares the photovoltaic parameters obtained in this work with representative experimentally reported $Sb_2Se_3$ thin-film solar cells. Such a comparison is useful for evaluating whether the proposed $In_2(O,S)_3$ buffer-layer strategy provides a meaningful improvement relative to experimentally demonstrated $Sb_2Se_3$ devices. It should be noted, however, that the present results are obtained from calibrated numerical simulation; therefore, the comparison should be interpreted as a performance-oriented benchmark rather than a direct replacement for experimental validation.

The optimized Mo/$MoSe_2$/$Sb_2Se_3$/$In_2S_{2.685}O_{0.315}$/ZnO/Al:ZnO device delivers $V_{oc}$ = 0.771 V, $J_{sc}$= 34.25 $mA\ cm^{-2}$, FF= 72.43%, and $\eta$= 19.12%. Compared with the experimentally calibrated reference device reported in Ref. [55], which exhibits $V_{oc}$= 0.48 V, $J_{sc}$= 30.86 $mA\ cm^{-2}$,FF= 67.19%, and $\eta$= 10.12%, the optimized Cd-free architecture shows simultaneous enhancement in all key photovoltaic parameters. The absolute efficiency improvement relative to this reference cell is:

$$\Delta\eta = \eta_{this\ work} - \eta_{reference} = 19.12\% - 10.12\% = 9.00\% \tag{32}$$

and the corresponding relative efficiency gain is:

$$Relative\ gain = \left[\frac{(\eta_{this\ work} - \eta_{reference})}{\eta_{reference}}\right] \times 100 = 88.9\% \tag{33}$$

**Table 4**
Comparison of $V_{oc}$, $J_{sc}$, Fill Factor (FF), and Efficiency (η) values from both experimental and simulation studies.

| Research Case | $V_{oc}$ (V) | $J_{sc}$ ($mA/cm^2$) | FF (%) | $\eta$ (%) | Reference |
|---|---|---|---|---|---|
| **Simulation** | **0.771** | **34.25** | **72.43** | **19.12** | **This work** |
| **Experimental** | 0.48 | 30.86 | 67.19 | 10.12 | [55] |
| **Experimental** | 0.38 | 26.24 | 57.82 | 5.95 | [37] |
| **Experimental** | 0.43 | 25.50 | 59.33 | 6.51 | [62] |
| **Experimental** | 0.32 | 26.6 | 43.5 | 3.92 | [63] |
| **Experimental** | 0.33 | 27.69 | 45.04 | 4.77 | [59] |
| **Experimental** | 0.42 | 29.9 | 60.4 | 7.6 | [64] |
| **Experimental** | 0.40 | 32.58 | 70.3 | 9.2 | [65] |
| **Experimental** | 0.40 | 25.14 | 55.7 | 5.6 | [29] |
| **Experimental** | 0.57 | 10.2 | 55.3 | 3.22 | [61] |
| **Experimental** | 0.40 | 25.69 | 64.78 | 6.71 | [27] |
| **Experimental** | 0.58 | 33.24 | 74.63 | 14.6 | [66] |

This substantial improvement originates mainly from the increase in $V_{oc}$ and $J_{sc}$, together with a moderate enhancement in FF. The higher $V_{oc}$ indicates suppressed recombination and improved quasi-Fermi-level splitting, while the increased $J_{sc}$ suggests reduced optical loss and improved carrier collection after replacing CdS with the optimized oxygen-alloyed $In_2(O,S)_3$ buffer.

Among the experimental reports listed in Table 4, the highest efficiency is 14.6%, with $V_{oc}$= 0.58 V, $J_{sc}$= 33.24 $mA\ cm^{-2}$, and FF= 74.63% [66]. The simulated efficiency of the optimized device in this work exceeds this value by 4.52 %age points. The relative enhancement with respect to this best experimental benchmark is [67]:

$$Relative\ gain = \left[\frac{(19.12 - 14.6)}{14.6}\right] \times 100 = 30.96\% \tag{34}$$

This comparison highlights the strong potential of composition-engineered $In_2(O,S)_3$ as a Cd-free buffer layer for $Sb_2Se_3$ photovoltaics. In particular, the optimized device achieves a higher $V_{oc}$ than all experimental cases listed in Table 4, confirming that band-offset control at the $Sb_2Se_3$/buffer interface is an effective route for reducing voltage loss. The $J_{sc}$ value of 34.25 $mA\ cm^{-2}$ is also among the highest values in the comparison, indicating that the wider-band-gap $In_2S_{2.685}O_{0.315}$ buffer can reduce front-side parasitic absorption while maintaining efficient carrier extraction. Although the FF remains slightly lower than the highest reported experimental FF of 74.63% [66], it is higher than most other reported values, suggesting that the optimized interface provides favorable charge selectivity and reduced transport loss.

In General, the benchmarking analysis confirms that the proposed Cd-free $Sb_2Se_3$/$In_2S_{2.685}O_{0.315}$ device offers a highly competitive simulated performance compared with reported experimental $Sb_2Se_3$ solar cells. More importantly, the improvement is not limited to a single output parameter; rather, it arises from the combined enhancement of $V_{oc}$, $J_{sc}$, and FF. These results further support the central conclusion of this study: precise oxygen-alloying in $In_2(O,S)_3$ can simultaneously improve optical transparency, optimize absorber/buffer band alignment, suppress interfacial recombination, and enable high-efficiency Cd-free $Sb_2Se_3$ thin-film solar cells.

### 3.7. Comparative assessment of the optimized architecture with and without an additional $TiO_2$ layer

To assess whether the optimized $In_2S_{2.685}O_{0.315}$ buffer benefits from an additional $TiO_2$ layer, the photovoltaic response of the proposed device was compared with that of its $TiO_2$-containing counterpart [68]. This comparison provides a complementary assessment of the device architecture by examining whether the favorable performance achieved through buffer-composition engineering can be further improved by introducing an additional layer into the front-side stack.

Fig. 12 compares the simulated illuminated J-V characteristics of the two configurations. The device without $TiO_2$ achieves a power conversion efficiency of 19.12%, with $V_{oc}$ = 0.771 V, $J_{sc}$ = 34.25 mA.cm$^{-2}$, and FF = 72.43%. In comparison, the $TiO_2$-containing configuration yields an efficiency of 18.26%, accompanied by $V_{oc}$ ≈ 0.76 V, $J_{sc}$ = 33.56 mA cm$^{-2}$, and FF = 71.15%. Accordingly, the $TiO_2$-free architecture exhibits an absolute efficiency advantage of 0.86 %age points, corresponding to approximately 4.71% higher efficiency relative to the $TiO_2$-containing device. The improvement involves all three photovoltaic parameters, indicating that the additional $TiO_2$ layer does not provide a net performance benefit under the investigated simulation conditions.

This result is consistent with the central design principle established by the composition-dependent analysis: device performance depends on the energetic compatibility and carrier-transport properties of the complete heterostructure, rather than on the number of functional layers alone. In the optimized device, the $In_2S_{2.685}O_{0.315}$ buffer already provides an almost flat conduction-band offset with $Sb_2Se_3$ ($\Delta E_c$ ≈

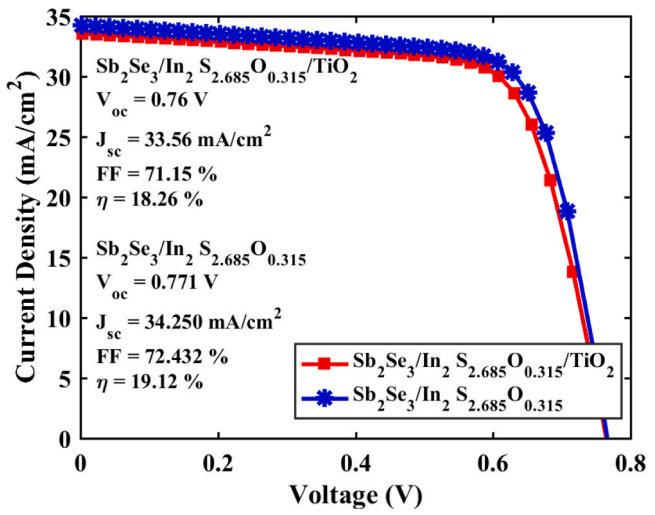


**Fig. 12.** Comparison of the simulated illuminated current-density–voltage characteristics of the optimized $Sb_2Se_3/In_2S_{2.685}O_{0.315}$ solar-cell configurations with and without an additional $TiO_2$ layer. The $TiO_2$-free device achieves a higher power conversion efficiency of 19.12%, compared with 18.26% for the $TiO_2$-containing configuration, together with higher $V_{oc}$, $J_{sc}$, and FF. The results support the $TiO_2$-free architecture under the investigated simulation conditions.

−0.01 eV), together with a substantial valence-band discontinuity. Within the adopted model, this combination supports electron extraction while restricting hole transfer into the front-side layers. An additional $TiO_2$ layer must therefore provide a compensating improvement in carrier selectivity or junction electrostatics to outweigh any additional optical attenuation, transport constraint, or interface-related loss.

The lower $J_{sc}$ and FF of the $TiO_2$-containing device are consistent with a less favorable net balance of carrier generation, collection, and transport, while the modest decrease in $V_{oc}$ indicates a change in the balance between photogeneration and recombination at open circuit. Nevertheless, the J–V comparison alone cannot uniquely distinguish among these contributions. In particular, attributing the efficiency reduction specifically to a $TiO_2$-induced conduction-band barrier or enhanced interfacial recombination would require supporting band-diagram, spatially resolved recombination, or spectral-response calculations for the $TiO_2$-containing structure.

The comparison therefore supports the selection of the $TiO_2$-free configuration as the preferred architecture within the investigated parameter set. It demonstrates that composition engineering of $In_2(O,S)_3$ can provide effective buffer functionality without requiring an additional $TiO_2$ layer, while retaining the higher simulated efficiency. This conclusion is specific to the modeled structures and material parameters; it does not imply that $TiO_2$ is intrinsically detrimental in other $Sb_2Se_3$ device configurations. Rather, Fig. 12 emphasizes that additional-layer incorporation should be justified by its net contribution to the performance of the complete device.

## 4. Conclusions

In this study, a calibrated SCAPS-1D model was employed to investigate Cd-free $Sb_2Se_3$ thin-film solar cells by replacing the conventional CdS buffer layer with composition-engineered $In_2(O,S)_3$. The model was first validated against the experimental EQE, integrated $J_{sc}$, light-intensity-dependent $J_{sc}$, and J-V characteristics of the reference $Sb_2Se_3$/CdS device, confirming its reliability for subsequent buffer-layer optimization.

The results demonstrate that oxygen alloying in $In_2(O,S)_3$ effectively modulates the buffer-layer bandgap, electron affinity, and conduction-band offset with $Sb_2Se_3$. Among the investigated compositions, $In_2S_{2.685}O_{0.315}$, corresponding to 1-x = 0.105, provided the most favorable nearly flat conduction-band alignment. This optimized interface suppressed cliff-induced recombination while preserving efficient electron extraction. Consequently, the Cd-free device achieved $V_{oc}$= 0.771 V, $J_{sc}$= 34.25 $mA\ cm^{-2}$, FF= 72.43%, and PCE= 19.12%, compared with 10.12% for the CdS-based reference cell.

The improved performance was further supported by capacitance-frequency, Mott-Schottky, and impedance analyses, which confirmed reduced charge accumulation, an enhanced built-in potential, and increased recombination resistance in the optimized device. Benchmarking against reported experimental $Sb_2Se_3$ solar cells further highlighted the potential of the proposed architecture, particularly in terms of $V_{oc}$ enhancement and overall efficiency improvement. In conclusion, this work demonstrates that composition-engineered $In_2(O,S)_3$ is a promising Cd-free buffer layer for $Sb_2Se_3$ photovoltaics, offering a physically grounded strategy to simultaneously reduce optical losses, optimize band alignment, suppress interfacial recombination, and improve device performance. Although the present study is based on a calibrated SCAPS-1D simulation framework, the observed trends provide practical design guidelines for the experimental development of composition-engineered $In_2(O,S)_3$ buffer layers in high-efficiency $Sb_2Se_3$ solar cells. Future experimental studies are encouraged to validate the predicted optimum oxygen composition, conduction-band alignment, and interface properties under realistic fabrication conditions.

## CRediT authorship contribution statement

**Danial Keighobadi:** Writing – original draft, Software, Investigation, Data curation, Conceptualization. **Mehdi Mousavi-Kamazani:** Validation, Supervision, Data curation, Conceptualization. **Mohammad Danaie:** Writing – review & editing, Supervision, Project administration, Formal analysis, Conceptualization.

## Ethical approval statement

The authors confirm that the submitted paper has not been submitted to any other journal and that this version is original and has not been published elsewhere. Additionally, all listed authors affirm the integrity of the study, data, information, and analyses, ensuring that no manipulations have been made. Furthermore, we confirm that no other individuals meet the authorship criteria for this paper beyond those listed as authors.

## Funding

The authors declare that no funds, grants, or financial support were received for the preparation of this manuscript.

## Declaration of Competing Interest

The authors declare that they have no known competing financial interests or personal relationships that could have appeared to influence the work reported in this paper.

## Data availability

Data will be made available on request.

## References

[1] B. Zhang, Z. Zeng, H. Dong, W. Gao, C. Ran, Recent advances in tin halide perovskite solar cells: a critical review, J. Mater. Chem. A 13 (37) (2025) 30708–30754.
[2] G. Yadav, M. Ahmaruzzaman, $CdIn_2S_4$-based advanced composite materials: structure, properties, and applications in environment and energy–A concise review, Inorg. Nano-Metal. Chem. 55 (2) (2025) 122–136.
[3] N. Asim, K. Sopian, S. Ahmadi, K. Saeedfar, M.A. Alghoul, O. Saadatian, S.H. Zaidi, A review on the role of materials science in solar cells, Renew. Sustain. Energy Rev. 16 (8) (2012) 5834–5847.

[4] D. Keighobadi, A.A. Orouji, M. Mousavi-Kamazani, M. Danaie, Enhanced performance of $Sb_2Se_3$-based solar cells with Fe doped $CuGa(S,Te)_2$ as a Secondary Absorber. Mater. Today Commun. 53 (2026) 115301.
[5] J.P. Tiwari, Flexible perovskite solar cells: a futuristic iots powering solar cell technology, short review, Small Methods 9 (1) (2025) 2400624.
[6] G. Tang, L. Chen, X. Cao, Y. Wang, H. Zhang, Q. Tai, A Review on recent advances in flexible perovskite solar cells, Sol. RRL 9 (5) (2025) 2400844.
[7] T.D. Lee, A.U. Ebong, A review of thin film solar cell technologies and challenges, Renew. Sustain. Energy Rev. 70 (2017) 1286–1297.
[8] P. Choubey, A. Oudhia, R. Dewangan, A review: Solar cell current scenario and future trends, Recent. Res. Sci. Technol. 4 (8) (2012).
[9] B. Asenjo, A.M. Chaparro, M.T. Gutierrez, J. Herrero, J. Klaer, Influence of $In_2S_3$ film properties on the behavior of $CuInS_2/In_2S_3/ZnO$ type solar cells, Sol. Energy Mater. Sol. Cells 87 (1-4) (2005) 647–656.
[10] S.M. Sivasankar, Progress in thin-film photovoltaics: a review of key strategies to enhance the efficiency of CIGS, CdTe, and CZTSSe solar cells, J. Compos. Sci. 9 (3) (2025) 143.
[11] A. Saidarsan, S. Guruprasad, A. Malik, P. Basumatary, D.S. Ghosh, A critical review of unrealistic results in SCAPS-1D simulations: causes, practical solutions and roadmap ahead, Sol. Energy Mater. Sol. Cells 279 (2025) 113230.
[12] A. Mavlonov, T. Razykov, F. Raziq, J. Gan, J. Chantana, Y. Kawano, T. Nishimura, H. Wei, A. Zakutayev, T. Minemoto, X. Zu, S. Li, L. Qiao, A review of $Sb_2Se_3$ photovoltaic absorber materials and thin-film solar cells, Sol. Energy 201 (2020) 227–246.
[13] D. Keighobadi, M. Mousavi-Kamazani, M. Danaie, Optimizing $Sb_2Se_3$ solar cells with $CdIn_2S_4$ buffer for high-efficiency and stability: a comprehensive analysis, Mater. Des. (2026) 115912.
[14] A. Yaqub, S.K. Yadav, A. Misra, A. Shukla, J. Singh, R.B. Singh, Design and optimization of an economic HTL-free, non-toxic double-layer perovskite solar cell for enhanced performance and stability, Int. J. Mater. Res. 116 (5) (2025) 402–415.
[15] S. Khatoon, et al., A simulation study of all inorganic lead-free $CsSnBr_3$ tin halide perovskite solar cell, Mater. Today. Proc. (2023).
[16] M.H. Miah, M.U. Khandaker, M.J. Hossen, Noor-E-Ashrafi, I. Jahan, M. Shahinuzzaman, M. Nur-E-Alam, M.Y. Hanfi, M.H. Ullah, M.A. Islam, Lead-free alternatives and toxicity mitigation strategies for sustainable perovskite solar cells: a critical review, Mater. Adv. 6 (9) (2025) 2718–2752.
[17] W. Akram, X. Li, S. Ahmed, Z. Ouyang, G. Li, A review of life cycle assessment and sustainability analysis of perovskite/Si tandem solar cells, RSC Sustain. 3 (1) (2025) 21–36.
[18] F. Mujtahid, P.L. Gareso, B. Armynah, D. Tahir, Review effect of various types of dyes and structures in supporting performance of dye-sensitized solar cell $TiO_2$-based nanocomposites, Int. J. Energy Res. 46 (2) (2022) 726–742.
[19] N. Kant, P. Singh, Review of next generation photovoltaic solar cell technology and comparative materialistic development, Mater. Today. Proc. 56 (2022) 3460–3470.
[20] D. Keighobadi, M. Mousavi-Kamazani, M. Danaie, Enhancing $Sb_2Se_3$ thin-film solar cell efficiency via $CuGaSe_2$ dual-absorber integration, Sci. Rep. 16 (2026) 34916.
[21] Q. Fatima, A.A. Haidry, H. Zhang, A. El Jery, M. Aldrdery, A critical review on advancement and challenges in using $TiO_2$ as electron transport layer for perovskite solar cell, Mater. Today Sustain. 27 (2024) 100857.
[22] Y. Wang, S. Ji, B. Shin, Interface engineering of antimony selenide solar cells: a review on the optimization of energy band alignments, J. Phys. Energy 4 (4) (2022) 044002.
[23] P. Roy, A. Ghosh, F. Barclay, A. Khare, E. Cuce, Perovskite solar cells: a review of the recent advances, Coatings 12 (8) (2022) 1089.
[24] K.O. Brinkmann, P. Wang, F. Lang, W. Li, X. Guo, F. Zimmermann, S. Olthof, D. Neher, Y. Hou, M. Stolterfoht, T. Wang, A.B. Djurišić, T. Riedl, Perovskite–organic tandem solar cells, Nat. Rev. Mater. 9 (3) (2024) 202–217.
[25] A. Bosio, G. Foti, S. Pasini, D. Spoltore, A review on the fundamental properties of $Sb_2Se_3$-based thin film solar cells, Energies 16 (19) (2023) 6862.
[26] Y. Gong, Q. Zhu, B. Li, S. Wang, B. Duan, L. Lou, C. Xiang, E. Jedlicka, R. Giridharagopal, Y. Zhou, Q. Dai, W. Yan, S. Chen, Q. Meng, H. Xin, Elemental de-mixing-induced epitaxial kesterite/CdS interface enabling 13%-efficiency kesterite solar cells, Nat. Energy 7 (10) (2022) 966–977.
[27] G. Li, Z. Li, X. Liang, C. Guo, K. Shen, Y. Mai, Improvement in $Sb_2Se_3$ solar cell efficiency through band alignment engineering at the buffer/absorber interface, ACS Appl. Mater. &nterfaces 11 (1) (2018) 828–834.
[28] Z. Zhao, Y. Cao, J. Yi, X. He, C. Ma, J. Qiu, Band-edge electronic structure of $\beta$-$In_2S_3$: the role of s or p orbitals of atoms at different lattice positions. ChemPhysChem 13 (6) (2012) 1551–1556.
[29] Y. Zhou, L. Wang, S. Chen, S. Qin, X. Liu, J. Chen, D.J. Xue, M. Luo, Y. Cao, Y. Cheng, E.H. Sargent, J. Tang, Thin-film $Sb_2Se_3$ photovoltaics with oriented one-dimensional ribbons and benign grain boundaries, Nat. Photonics 9 (6) (2015) 409–415.
[30] M. Burgelman, K. Decock, S. Khelifi, A. Abass, Advanced electrical simulation of thin film solar cells, Thin Solid. films 535 (2013) 296–301.
[31] Y. Seminovski, P. Palacios, P. Wahnón, R. Grau-Crespo, Band gap control via tuning of inversion degree in $CdIn_2S_4$ spinel, Appl. Phys. Lett. 100 (10) (2012).
[32] J.V. Li, X. Li, D.S. Albin, D.H. Levi, A method to measure resistivity, mobility, and absorber thickness in thin-film solar cells with application to CdTe devices, Sol. Energy Mater. Sol. Cells 94 (12) (2010) 2073–2077.
[33] Q. Zhao, R. Tang, B. Che, Y. He, T. Wu, X. Peng, J. Yang, S. Sheng, C. Zhu, T. Chen, Grain-boundary elimination via liquid medium annealing toward high-efficiency $Sb_2Se_3$ Solar Cells, Adv. Mater. 37 (4) (2025) 2414082.
[34] S. Zhang, C. Wu, J. Zeng, X. Meng, R. Hu, J. Wang, K. Chen, Grain size and absorber thickness than solely controlling orientation for fabricating high-performance $Sb_2Se_3$ solar cells, J. Phys. Chem. Lett. 16 (35) (2025) 8928–8935.
[35] C. Zhang, R. Jiang, Y. Zheng, Y. Li, Z. Cai, C. Ma, Y. Cheng, J. Chu, J. Tao, Mechanism of defect passivation in $Sb_2Se_3$ solar cells via buried selenium seed layer, Adv. Energy Mater. 15 (7) (2025) 2403352.
[36] M. Minbashi, A. Ghobadi, M.H. Ehsani, H. Rezagholipour Dizaji, N. Memarian, Simulation of high efficiency SnS-based solar cells with SCAPS, Sol. Energy 176 (2018) 520–525.
[37] L. Wang, D.B. Li, K. Li, C. Chen, H.X. Deng, L. Gao, Y. Zhao, F. Jiang, L. Li, F. Huang, Y. He, H. Song, G. Niu, J. Tang, Stable 6%-efficient $Sb_2Se_3$ solar cells with a ZnO buffer layer, Nat. Energy 2 (4) (2017) 17046.
[38] M. Minbashi, M.K. Omrani, N. Memarian, D.H. Kim, Comparison of theoretical and experimental results for band-gap-graded CZTSSe solar cell, Curr. Appl. Phys. 17 (10) (2017) 1238–1243.
[39] F. Yousaf, et al., The path to increase $Sb_2Se_3$ solar cell efficiency: a numerical approach into loss mechanisms, J. Phys. Chem. Solids (2025) 113443.
[40] A. Mo, B. Yang, X. Lu, Y. Duan, X. Liang, Z. Zhang, Y. Guo, Z. Li, Reducing parasitic loss and deep defect formation via copper doping toward highly efficient $Sb_2Se_3$ solar cells, Adv. Funct. Mater. 35 (20) (2025) 2420261.
[41] G. Lim, V.Q. Hoang, J. Lee, J.K. Kang, K.J. Yang, S.J. Sung, D.H. Kim, W. Jo, Advanced interfacial charge carrier transport enabling the improvement of open-circuit voltage in $Sb_2Se_3$ solar cells, J. Mater. Chem. A 13 (15) (2025) 10622–10629.
[42] G. Lim, V.Q. Hoang, J. Lee, J.K. Kang, K.J. Yang, S.J. Sung, D.H. Kim, W. Jo, Advanced interfacial charge carrier transport enabling the improvement of open-circuit voltage in $Sb_2Se_3$ solar cells, J. Mater. Chem. A 13 (2025) 10622–10629.
[43] S. Ramírez-Velasco, J.R. González-Castillo, F. Ayala-Mató, V. Hernández-Calderón, D. Jiménez-Olarte, O. Vigil-Galán, Back contact modification in $Sb_2Se_3$ solar cells: the effect of a thin layer of $MoSe_2$, Thin Solid. Films 751 (2022) 139227.
[44] Z.-S. Wang, H. Kawauchi, T. Kashima, H. Arakawa, Significant influence of $TiO_2$ photoelectrode morphology on the energy conversion efficiency of N719 dye-sensitized solar cell, Coord. Chem. Rev. 248 (13-14) (2004) 1381–1389.
[45] A. Ait Abdelkadir, et al., Numerical simulation and optimization of n-Al-ZnO/n-CdS/p-CZTSe/p-NiO (HTL)/Mo solar cell system using SCAPS-1D, Results Opt. 8 (2022) 100257.
[46] J. Xia, Q. Wang, M. Wei, L. Chen, N. Liu, S. Fan, H. Wu, In situ grown $NiIn_2S_4$ nanosheets as counter electrode for bifacial quasi-solid-state dye-sensitized solar cells, J. Mater. Sci. 56 (3) (2021) 2372–2384.
[47] W.-B. Yuan, T. Yuan, J. Shen, C.M. Yang, L. Hu, Two-dimensional $In_2S_2Se/In_2Se_3$ vdWH: solar cell material with high power conversion efficiency, Phys. Scr. 101 (2026) 035907.
[48] W. Li, X.F. Cai, N. Valdes, T. Wang, W. Shafarman, S.H. Wei, A. Janotti, $In_2Se_3$, $In_2Te_3$, and $In_2(Se,Te)_3$ alloys as photovoltaic materials, J. Phys. Chem. Lett. 13 (51) (2022) 12026–12031.
[49] Cd Groot, J. Moodera, Growth and characterization of a novel $In_2Se_3$ structure, J. Appl. Phys. 89 (8) (2001) 4336–4340.
[50] E. Ghorbani, X. Jin, D. Perera, R. Schneider, D. Gerthsen, D. Hariskos, R. Menner, W. Witte, K. Albe, Influence of oxygen content on the properties of $In_2(O_xS_{1-x})_3$ used as buffer material in $Cu(In,Ga)Se_2$ solar cells, J. Appl. Phys. 135 (7) (2024).
[51] N. Barreau, S. Marsillac, J.C. Bernède, L. Assmann, Evolution of the band structure of $\beta$-$In_2S_{3-3x}O_{3x}$ buffer layer with its oxygen content, J. Appl. Phys. 93 (9) (2003) 5456–5459.
[52] N. Barreau, S. Marsillac, D. Albertini, J.C. Bernede, Structural, optical and electrical properties of $\beta$-$In_2S_{3-3x}O_{3x}$ thin films obtained by PVD, Thin Solid. Films 403 (2002) 331–334.
[53] Y. Singh, S. Rani, Shashi, R. Parmar, R. Kumari, M. Kumar, A. Bala Sairam, Mamta, V.N. Singh, $Sb_2Se_3$ heterostructure solar cells: techniques to improve efficiency, Sol. Energy 249 (2023) 174–182.
[54] A.S.R. Bati, Y.L. Zhong, P.L. Burn, M.K. Nazeeruddin, P.E. Shaw, M. Batmunkh, Next-generation applications for integrated perovskite solar cells, Commun. Mater. 4 (1) (2023) 2.
[55] Z. Duan, X. Liang, Y. Feng, H. Ma, B. Liang, Y. Wang, S. Luo, S. Wang, R.E. I. Schropp, Y. Mai, Z. Li, $Sb_2Se_3$ thin-film solar cells exceeding 10% power conversion efficiency enabled by injection vapor deposition technology, Adv. Mater. 34 (30) (2022) 2202969.
[56] D. Keighobadi, S. Mohammadi, Modeling of drain current in double-gate heterojunction tunneling FETs: a physical-analytical approach, Model. Simul. Electr. Electron. Eng. 1 (3) (2021) 1–7.
[57] R. Venkatesh, Magnesium alloy and silicon nitrides composite study: synthesis and abrasive water jet machining behavior and optimization, SAE Int. J. Mater. Manuf. 18 (2) (2024) 191–198.
[58] R. Venkatesh, Machining parameter optimization and study the turning operation behaviour of hybrid Al/Mg composites, Jordan. J. Mech. Ind. Eng. 18 (4) (2024) 711.
[59] K. Yang, B. Li, G. Zeng, $Sb_2Se_3$ thin film solar cells prepared by pulsed laser deposition, J. Alloy. Compd. 821 (2020) 153505.
[60] S. Mohammadi, D. Keighobadi, A universal analytical potential model for double-gate Heterostructure tunnel FETs, IEEE Trans. Electron. Devices 66 (3) (2019) 1605–1612.
[61] H. Deng, S. Yuan, X. Yang, F. Cai, C. Hu, K. Qiao, J. Zhang, J. Tang, H. Song, Z. He, Efficient and stable $TiO_2/Sb_2S_3$ planar solar cells from absorber crystallization and Se-atmosphere annealing, Mater. Today Energy 3 (2017) 15–23.
[62] C. Chen, L. Wang, L. Gao, D. Nam, D. Li, K. Li, Y. Zhao, C. Ge, H. Cheong, H. Liu, H. Song, J. Tang, 6.5% certified efficiency $Sb_2Se_3$ solar cells using PbS colloidal

quantum dot film as hole-transporting layer, ACS Energy Lett. 2 (9) (2017) 2125–2132.
[63] X. Wen, Y. He, C. Chen, X. Liu, L. wang, B. Yang, M. Leng, H. Song, K. Zeng, D. Li, K. Li, L. Gao, J. Tang, Magnetron sputtered ZnO buffer layer for $Sb_2Se_3$ thin film solar cells, Sol. Energy Mater. Sol. Cells 172 (2017) 74–81.
[64] X. Wen, C. Chen, S. Lu, K. Li, R. Kondrotas, Y. Zhao, W. Chen, L. Gao, C. Wang, J. Zhang, G. Niu, J. Tang, Vapor transport deposition of antimony selenide thin film solar cells with 7.6% efficiency, Nat. Commun. 9 (1) (2018) 2179.
[65] Z. Li, X. Liang, G. Li, H. Liu, H. Zhang, J. Guo, J. Chen, K. Shen, X. San, W. Yu, R. Schropp, Y. Mai, 9.2%-efficient core-shell structured antimony selenide nanorod array solar cells, Nat. Commun. 10 (1) (2019) 125.
[66] H. Jalali, A.A. Orouji, I. Gharibshahian, Controlled conduction band offset in $Sb_2Se_3$ solar cell through introduction of (Zn,Sn)O buffer layer to improve photovoltaic performance: a simulation study, Sol. Energy Mater. Sol. Cells 260 (2023) 112492.
[67] D. Keighobadi, A.A. Orouji, M. Mousavi-Kamazani, M. Danaie, $Sb_2Se_3$/$MAPbI_3$ thin-film solar cells: interface engineering and performance enhancement, Results Eng. 32 (2026) 112560.
[68] E.M. Haghighi, A.A. Orouji, Optimizing interface energy band alignment in Cd-free $Sb_2Se_3$ solar cells by controlling the oxygen content of $In_2(O,S)_3$ buffer layer to improve the efficiency: a simulation study, Opt. Laser Technol. 169 (2024) 110107.